

Numerical and Perturbative Computations of the Fuzzy Dark Matter Model

Xinyu Li* and Lam Hui†

Center for Theoretical Physics, Department of Physics, Columbia University, New York, NY 10027

Greg L. Bryan‡

Department of Astronomy, Columbia University, New York, NY 10027
Center for Computational Astrophysics, Flatiron Institute, New York, NY 10003

(Dated: October 5, 2018)

We investigate nonlinear structure formation in the fuzzy dark matter (FDM) model using both numerical and perturbative techniques. On the numerical side, we examine the virtues and limitations of a Schrödinger-Poisson solver (wave formulation) versus a fluid dynamics solver (Madelung formulation). On the perturbative side, we carry out a computation of the one-loop mass power spectrum, i.e. up to third order in perturbation theory. We find that (1) in many situations, the fluid dynamics solver is capable of producing the expected interference patterns, but it fails in situations where destructive interference causes the density to vanish – a generic occurrence in the nonlinear regime. (2) The Schrödinger-Poisson solver works well in all test cases, but it is demanding in resolution: suppose one is interested in the mass power spectrum on large scales, it's not sufficient to resolve structure on those same scales; one must resolve the relevant de Broglie scale which is often smaller. The fluid formulation does not suffer from this issue. (3) We compare the one-loop mass power spectrum from perturbation theory against the mass power spectrum from the Schrödinger-Poisson solver, and find good agreement in the mildly nonlinear regime. We contrast fluid perturbation theory with wave perturbation theory; the latter has a more limited range of validity. (4) As an application, we compare the Lyman-alpha forest flux power spectrum obtained from the Schrödinger-Poisson solver versus one from an N-body simulation (the latter is often used as an approximate method to make predictions for FDM). At redshift 5, the two, starting from the same initial condition, agree to better than 10% on observationally relevant scales as long as the FDM mass exceeds 2×10^{-23} eV. We emphasize that the so called quantum pressure is capable of both enhancing and suppressing fluctuations in the nonlinear regime - which dominates depends on the scale and quantity of interest.

I. INTRODUCTION

The fuzzy dark matter (FDM) model posits that dark matter consists of an ultra-light boson with a macroscopic de Broglie wavelength [1–5]. A pseudo Nambu-Goldstone boson is a fairly natural candidate for such a particle, for instance an axion-like particle.¹ The axion ϕ is an angular field with a periodicity of $2\pi F$, where F is often called the axion decay constant. Non-perturbative effects give rise to a potential, breaking the shift symmetry expected for a Goldstone boson to a discrete symmetry $\phi \rightarrow \phi + 2\pi F$. Assuming a primordial value of order F , the axion goes from being frozen in the early universe to oscillating in the late universe, leading to a relic abundance of [6–8]:

$$\Omega_{\text{axion}} \sim 0.1 \left(\frac{F}{10^{17} \text{ GeV}} \right)^2 \left(\frac{m}{10^{-22} \text{ eV}} \right)^{1/2}, \quad (1)$$

where m is the axion mass. The abundance is more sensitive to the value of F than to m . Axion candidates in string theory typically span $F \sim 10^{16} - 10^{18}$ GeV [9]. There is thus quite a wide range in m that gives the desired abundance for dark matter. Interestingly, the rather low m suggested by this argument predicts a number of astrophysical effects that are potentially observable, spanning the linear regime (see the seminal paper by Hu *et al.* [2] who coined the term fuzzy dark matter) and the nonlinear one [8, 10–18].

For most applications, the non-relativistic approximation is adequate – a complex scalar ψ is introduced that relates to the real axion field ϕ as follows:

$$\phi = \sqrt{\frac{\hbar^3}{2m}} \left(\psi e^{-imt/\hbar} + \psi^* e^{imt/\hbar} \right), \quad (2)$$

where we set the speed of light $c = 1$, but keep \hbar explicit. Assuming $|\dot{\psi}| \ll m|\psi|$, the Klein-Gordon equation² for the axion ϕ reduces to the Schrödinger equation for ψ :

$$i\hbar \left(\partial_t \psi + \frac{3}{2} H \psi \right) = \left(-\frac{\hbar^2}{2ma^2} \nabla^2 + m\Phi \right) \psi, \quad (3)$$

* xinyu.li@columbia.edu

† lhui@astro.columbia.edu

‡ gbryan@astro.columbia.edu

¹ For the purpose of this article, it is not crucial that FDM is an axion or axion-like particle. The main ingredient we assume is that the particle is bosonic, non-relativistic and can be approximated as free except for gravitational interaction. The advantage of thinking of the FDM as an axion is that the relic abundance naturally takes the desired value, under mild assumptions.

² For most applications, the self-interaction of the axion can be ignored. Thus, the predictions for structure formation are identical to that of a light, free scalar.

where t is proper time, the spatial derivative is with respect to comoving coordinates, a is the scale factor, $H \equiv \dot{a}/a$ is the Hubble parameter and Φ is the gravitational potential, obeying:

$$\nabla^2 \Phi = 4\pi G a^2 \bar{\rho} \delta \quad (4)$$

where $\bar{\rho}$ is the cosmic mean mass density and δ is the overdensity. We use $\dot{}$ to denote a derivative with respect to proper time t . Note that:

$$\bar{\rho} = m\bar{\psi}^2, \quad \rho = m|\psi|^2, \quad \delta \equiv (\rho - \bar{\rho})/\bar{\rho}, \quad (5)$$

where $\bar{\psi}$ is chosen to be real without loss of generality.

The Schrödinger-Poisson system of wave dynamics (3) and (4) can be recast as fluid dynamics (known as the Madelung formulation [19], see the Feynman lectures for a discussion [20]). The field ψ is related to the fluid mass density ρ as above, and the fluid velocity \mathbf{v} as follows:

$$\psi \equiv \sqrt{\frac{\rho}{m}} e^{i\theta}, \quad \mathbf{v} \equiv \frac{\hbar}{ma} \nabla \theta. \quad (6)$$

With this mapping, the conservation associated with the $U(1)$ symmetry of the Schrödinger equation (which originates from particle number conservation in the non-relativistic limit) becomes mass conservation:

$$\dot{\rho} + 3H\rho + \frac{1}{a} \nabla \cdot (\rho \mathbf{v}) = 0, \quad (7)$$

and the conjugate part of the Schrödinger equation gives the analog of the Euler equation:

$$\dot{\mathbf{v}} + H\mathbf{v} + \frac{1}{a} (\mathbf{v} \cdot \nabla) \mathbf{v} = -\frac{1}{a} \nabla \Phi - \frac{\hbar^2}{2m^2 a^3} \nabla p, \quad (8)$$

where

$$p \equiv -\frac{\nabla^2 \sqrt{\rho}}{\sqrt{\rho}} = -\frac{1}{2} \nabla^2 \log \rho - \frac{1}{4} (\nabla \log \rho)^2. \quad (9)$$

The quantity p is often referred to as “quantum pressure”. This is a bit of a misnomer (which we adopt nonetheless, following convention) — it is in fact not a pressure, but arises from some particular combination of stress i.e. the stress tensor in general has non-vanishing off-diagonal terms.³

In the fluid formulation, \hbar can be grouped together with m to define a length scale (the Compton scale \hbar/m), after which \hbar does not appear in the rest of the equations (7) and (8). In the applications we are interested in, the relevant particle number occupancy is large, making quantum fluctuations very small. The Schrödinger equation, despite its appearance, should be interpreted as an equation for a classical complex scalar ψ (though we will adhere to the common terminology of ψ as the

wave function). Wave mechanics effects such as interference are still present, since $\rho = m|\psi|^2$, but they are classical in nature, much like the interference of waves in classical electromagnetism.

In the literature, there are investigations of structure formation in the FDM model using both the wave formulation [10, 13, 15, 21] and the fluid formulation [12, 14, 18, 22]. Our goal is to build on and extend these investigations in a number of ways. (1) We investigate the strengths and weaknesses of solvers based on the wave and fluid formulations by studying test cases. (2) We carry out perturbative computations (in the fluid formulation, for reasons that will become clear) up to third order in perturbation theory, and compare the results against numerical solutions. (3) As an application, we numerically compute the Lyman-alpha forest flux power spectrum in the FDM model, and compare the prediction from solving the Schrödinger-Poisson system versus the prediction from a pure gravity solver (starting from the same initial conditions). Current constraints on the FDM mass from the Lyman-alpha forest use N-body simulations (i.e. a gravity solver) to approximate the dynamics [23, 24]⁴, and we address the question of how the predictions are sensitive to the presence/absence of quantum pressure.

The paper is organized as follows. In Sec. II, we summarize perturbation theory results that are presented in more details in the Appendix. The perturbative computation provides a number of insights that are useful for interpreting the numerical results. In Sec. III, we describe our code SPoS, a second order Schrödinger-Poisson solver and compare it with a grid-based fluid solver that incorporates quantum pressure. We go over the pros and cons of both, and show the fluid formulation fails in cases where the density vanishes due to chance destructive interference (which seem to generically occur in the highly nonlinear regime). Certain details of the fluid solver are relegated to the Appendix. In Sec. IV, we apply the Schrödinger-Poisson solver to compute the Lyman-alpha forest flux power spectrum, and quantify how the predictions differ if one were to approximate the dynamics as purely gravitational (i.e. FDM versus CDM dynamics, from the same initial conditions).

In sample cosmological calculations, the parameters used are: density parameters for dark matter $\Omega_{m,0} = 0.268$, dark energy $\Omega_{\Lambda,0} = 0.732$, the Hubble constant in unit 100 /km/s/Mpc $H_0 = 0.704$, the fluctuation amplitude $\sigma_8 = 0.811$, the spectral index $n_s = 0.961$ and the CMB temperature today $T_{CMB} = 2.726$ K. Our cosmological numerical simulations start at $z = 100$.

As this article was under preparation, a paper by Nori et al. [25] appeared that has some overlap with this one, in particular regarding the Lyman-alpha forest.

³ The stress tensor takes a special form such that its divergence divided by density takes the form of the spatial gradient of p .

⁴ An exception is [22] who incorporated quantum pressure in their simulations. As we will see below, incorporating quantum pressure in a fluid formulation has issues that need to be addressed.

II. PERTURBATIVE COMPUTATIONS OF THE FDM MODEL

There are two possible perturbative computations, one in the fluid formulation and one in the wave formulation. We summarize the main results in this section, and relegate the details to Appendices B and C.

In the wave formulation, one expands in small perturbation to the wave function: $\delta\psi/\bar{\psi}$. In the fluid formulation, one expands in small overdensity $\delta \equiv (\rho - \bar{\rho})/\bar{\rho}$ and peculiar velocity v . To linear order, they are related by:

$$\delta = (\delta\psi + \delta\psi^*)/\bar{\psi}, \quad (10)$$

and

$$\mathbf{v} = \frac{\hbar}{2iam\bar{\psi}} \nabla(\delta\psi - \delta\psi^*). \quad (11)$$

The latter in momentum space reads:

$$\frac{\delta\psi - \delta\psi^*}{\bar{\psi}} \sim \frac{amv}{\hbar k}. \quad (12)$$

where k is the (comoving) momentum. The regime of validity in wave perturbation theory is thus different from that in fluid perturbation theory. For fluid perturbation theory, δ and v ought to be small. For wave perturbation theory, the smallness of the real part of $\delta\psi/\bar{\psi}$ is equivalent to the smallness of δ , but the smallness of the imaginary part requires $v \ll \hbar k/(am)$. Since the physical length scale of interest a/k is generally longer than the Compton scale \hbar/m , the latter requirement is more stringent than simply requiring a small v . To put it in another way, wave perturbation theory requires $a/k \ll \hbar/(mv)$ i.e. the proper length scale of interest must be shorter than the de Broglie scale:

$$\frac{\lambda_{\text{deB.}}}{2\pi} \equiv \frac{\hbar}{mv} = 1.92 \text{ kpc} \left(\frac{10^{-22} \text{ eV}}{m} \right) \left(\frac{10 \text{ km/s}}{v} \right). \quad (13)$$

This is a rather demanding requirement: for a given comoving k , wave perturbation theory generally breaks down at an earlier time than fluid perturbation theory (see Appendix C).

We therefore focus on fluid perturbation theory in the rest of the paper. We compute the predictions up to third order in perturbation, and derive the one-loop corrections to the mass power spectrum (Appendix B). Let's consider the right hand side of the Euler equation (8) - taking its divergence and using the Poisson equation (4):

$$\begin{aligned} \text{R. H. S.} &= -4\pi G\bar{\rho}a\delta \\ &+ \frac{\hbar^2}{4a^3m^2} \nabla^2 \left(\nabla^2\delta - \frac{1}{4}\nabla^2\delta^2 - \frac{1}{2}\delta\nabla^2\delta + \right. \\ &\quad \left. \frac{1}{8}\nabla^2\delta^3 + \frac{3}{8}\delta^2\nabla^2\delta + \frac{1}{8}\delta\nabla^2\delta^2 + \dots \right) \end{aligned} \quad (14)$$

To linear order in δ , as noted by [2], the quantum pressure leads to a suppression of growth on small length

scales (large momenta). The characteristic momentum where the quantum pressure term balances gravity is k_{Jeans} , the (comoving) Jeans scale (Appendix B):

$$k_{\text{Jeans}} \equiv \frac{44.7}{\text{Mpc}} \left(6a \frac{\Omega_{m0}}{0.3} \right)^{1/4} \left(\frac{H_0}{70 \text{ km/s}} \frac{m}{10^{-22} \text{ eV}} \right)^{1/2} \quad (15)$$

Eqn. (14) shows that the second order terms from the quantum pressure could act in the *same* direction as gravity, enhancing rather than suppressing fluctuations. Consider the example of a density peak with $\delta > 0$ a Gaussian profile, it is straightforward to check that, at the peak, the second order contributions to quantum pressure act in an opposite way to the first order contribution. Of course, once the second order terms become important, one has to consider the higher order terms as well which could yet reverse the sign of the effect - in such a case, the perturbative expansion cannot be counted on to give the correct predictions and one has to resort to numerical computations. Nonetheless, this exercise shows that in the nonlinear regime, it is by no means guaranteed that quantum pressure leads to a suppression of fluctuations (see further discussions in Appendix B).

Interestingly, the wave formulation offers useful insights in the nonlinear regime. In a (non-solitonic) halo which consists of a superposition of waves of different momenta, the fact that $\rho \propto |\psi|^2$ sets up the opportunity for interference effects. A chance superposition could lead to local constructive or destructive interference, causing sizable density fluctuations on the de Broglie scale. This is borne out by numerical simulations of FDM halos [10, 11].

Let us close this section with a sample computation of the mass power spectrum up to one-loop, that is, including corrections to the power spectrum that are quadratic in the linear power spectrum (Appendix B).

The tree (linear) power spectrum at redshift $z = 5$ for an FDM particle mass of 10^{-23} eV is shown in the lower panel of Fig. 1 (the lower dashed blue line). The tree power spectrum at the same redshift and with the same initial condition but CDM dynamics is shown as the lower solid blue line in the same panel. The fact that they are very similar is due to the fact that the linear growth factor D_k does not differ a whole lot between FDM and CDM dynamics for $k < 10$ h/Mpc. (Recall from Eqn. (15) that $k_{\text{Jeans}} \sim 14 \text{ Mpc}^{-1}$ for a mass of 10^{-23} eV and $a = 1/6$.) In other words, the suppression of power seen in Fig. 1 at high momenta has nothing to do with the low redshift FDM dynamics; it's all in the initial condition. Indeed, the scale at which the initial or primordial power spectrum is suppressed by a factor of two is [2]:

$$k_{1/2} = \frac{1.62}{\text{Mpc}} \left(\frac{m}{10^{-23} \text{ eV}} \right)^{4/9}. \quad (16)$$

This is substantially smaller (i.e. longer length scale) than k_{Jeans} at $z = 5$. Thus, based on linear perturbation theory alone, we do not expect CDM and FDM dynamics to give vastly different power spectra starting from

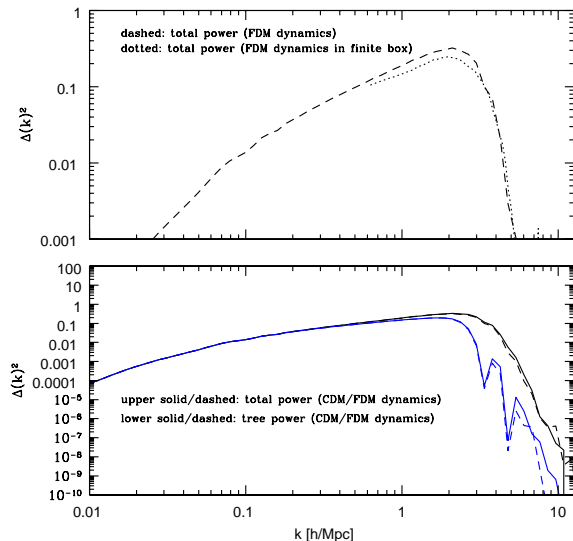


FIG. 1. *Lower panel:* the upper solid/dashed (black) lines give the $z = 5$ total power (tree + 1-loop) under CDM/FDM dynamics respectively. The initial condition is the same in both cases, corresponding to an FDM mass of 10^{-23} eV. The lower solid/dashed (blue) lines gives the $z = 5$ tree power under CDM/FDM dynamics. *Upper panel:* the dashed line is the $z = 5$ total power under FDM dynamics (identical to the upper dashed line in the lower panel); the dotted line is the total power if the tree power spectrum is cut-off at $k < 2\pi/10$ h/Mpc, which limits the transfer of power from low momenta to high momenta through the loop integrals (accounting for the effect of a finite box size of 10 Mpc/h). Here, $\Delta(k)^2 \equiv 4\pi k^3 P(k)/(2\pi)^3$ represents the dimensionless power.

the same initial condition. The question is whether this persists at higher order in perturbation theory.

Fig. 1 lower panel shows the total (tree + one-loop) power: the upper solid (black) line uses CDM dynamics while the upper dashed (black) line uses FDM dynamics (same initial condition). The power is enhanced at high momenta compared with the tree power spectrum (the lower solid/dashed blue lines). The power at $k \gtrsim k_{1/2}$ comes almost entirely from transferred power from large scales (low momenta). Just as in the case of the tree power, CDM vs FDM dynamics does not appear to make a big difference in the total power. The total power with FDM dynamics is slightly lower than that with CDM dynamics, except possibly at $k \sim 10$ h/Mpc, though at that point, the power spectrum is rather low in any case (due to the suppression of high k power in the initial condition). One main goal of the following section is to investigate using numerical simulations to what extent these conclusions remain valid in the fully nonlinear regime.

As we will see below, numerical simulations place twin demands on resolution and box size that can be challenging to satisfy. Perturbative calculation is useful for gauging the effect of a finite box size. Fig. 1 upper

panel compares the total power in two cases (both with FDM dynamics): the dashed line is the same as the black dashed line (power spectrum up to one-loop) in the lower panel; the dotted line shows also the power up to one-loop, except the loop integral is computed with an infrared cut-off at momentum $2\pi/10$ h/Mpc. The latter is chosen to mimic the effect of having a finite simulation box of size 10 Mpc/h. One can see the transferred power from large scales is diminished, because the relevant large scale modes are absent in a finite box. We will return to this issue of a finite box size in our numerical computations.

III. NUMERICAL COMPUTATIONS OF THE FDM MODEL

In this section, we turn to numerical computations. Just as in the case of perturbative calculations, one can integrate the Schrödinger-Poisson system Eqn. (3) and (4) or the fluid-Poisson system Eqn. (4), (7) and (8).

The advantage of the fluid-Poisson system is that working hydrodynamics codes already exist. The quantum pressure term p encodes the effects of wave dynamics, such as interference. This is borne out by tests we have performed, detailed in Appendix A (see e.g. Fig. 11). Problems arise, however, in test cases where the density vanishes at isolated points, which naturally occur due to chance destructive interference in the wave language. The quantum pressure is ill-defined in these regions. One might hope that these isolated problematic points do not affect the overall evolution, but they can, as illustrated in the example of Fig. 12. It is conceivable that a fluid code can be suitably modified to integrate across these regions of vanishing density. We defer this to a future discussion. We will instead largely focus on a numerical code that solves the Schrödinger-Poisson system, though in a few examples, we will contrast the performance of the fluid and the wave codes. Let us also mention the possibility of a hybrid approach that combines the best features of both formulations, for instance a fluid solver on large scales and a wave solver on small scales (see further discussions below). An example is given by [17] who used the combination of an N-body code and a Schrödinger-Poisson solver.

A. Description of SPoS (Schrödinger-Poisson Solver)

By defining a normalized wave function $\tilde{\psi} \equiv a^{3/2}\psi$, the Schrödinger-Poisson equation for FDM dynamics takes the following form

$$\frac{\partial \tilde{\psi}}{\partial t} = (K + V)\tilde{\psi} \equiv \left(i \frac{\hbar}{ma^2} \nabla^2 - i \frac{m}{\hbar} \Phi \right) \tilde{\psi}, \quad (17)$$

where $K = i \frac{\hbar}{ma^2} \nabla^2$ is the kinetic operator and $V = -im\Phi/\hbar$ is the potential operator. Our SPoS code inte-

grates Eqn. (17) using an operator split method similar to [15, 21]. The operator split method follows the observation that the unitary time evolution operator can be split in the following way to give second order accuracy in time (i.e. corrections are third order):

$$\begin{aligned}\tilde{\psi}(t + \Delta t) &= e^{(K+V)\Delta t}\tilde{\psi}(t) \\ &= e^{V\Delta t/2}e^{K\Delta t}e^{V\Delta t/2}\tilde{\psi}(t) + \mathcal{O}(\Delta t^3).\end{aligned}\quad (18)$$

Therefore, for each time step Δt , our SPoS code evolves $\tilde{\psi}$ in the following three sub-steps. In the first sub-step, $\tilde{\psi}$ is evolved with the gravitational potential operator for $\Delta t/2$:

$$\tilde{\psi} \rightarrow \exp\left(-i\frac{m}{\hbar}\Phi\frac{\Delta t}{2}\right)\tilde{\psi}.\quad (19)$$

In the second sub-step, the kinetic operator is applied to $\tilde{\psi}$ using the 4th order Runge-Kutta method for time integration with a 4th order finite difference method for spatial derivatives

$$\tilde{\psi} \rightarrow \tilde{\psi} + i\frac{\hbar}{ma^2}\nabla^2\tilde{\psi}\Delta t.\quad (20)$$

Finally, ψ is evolved with the gravitational potential for another $\Delta t/2$ to finish a full time step of evolution.

The time step Δt is set by respecting the Courant-Friedrichs-Lewy (CFL) condition for a parabolic system with cell size Δx and requiring the phase change in the gravitational potential step is smaller than unity i.e.

$$\Delta t < \min\left[\frac{ma^2}{6\hbar}\Delta x^2, \frac{\hbar}{m\Phi}\right].\quad (21)$$

The SPoS code is built as a module into the ENZO code [26] for cosmological simulations with existing modules to calculate the cosmological expansion and gravitational potential; some analysis below is carried out with the YT package [27].

B. Tests of SPoS (and Comparisons with a Fluid Solver)

The Schrödinger-Poisson solver is very demanding in terms of resolution. Recall that the velocity is related to the gradient of the phase of the wave function, i.e. a given velocity translates into a phase that varies on the scale of the de Broglie wavelength. It is thus important the de Broglie scale is resolved; otherwise the velocity field is not represented correctly. This is true even if the scale of interest is much larger than the de Broglie scale. This is illustrated in Fig. 2.

The matter (mass) power spectrum is shown for FDM dynamics corresponding to a mass of 10^{-23} eV and 10^{-22} eV on the left and right panel of Fig. 2 respectively.⁵ In

both cases, the simulation box size is 10 Mpc/h comoving, with a 1024^3 grid (the Nyquist frequency is about 600 h/Mpc comoving). The resolution is adequate to resolve the de Broglie scale for the case of 10^{-23} eV but not for 10^{-22} eV. One can estimate the de Broglie scale by using the velocity dispersion on the scale of the box (comoving) 10 Mpc/h. At $z = 5$, this is about 100 km/s, giving a (physical or proper) de Broglie scale of about 2 kpc for $m = 10^{-23}$ eV and 0.2 kpc for $m = 10^{-22}$ eV (Eqn. 13). Contrast this with the simulation resolution, which is about 2 kpc (proper) at $z = 5$. Thus the de Broglie scale is marginally resolved for $m = 10^{-23}$ eV but certainly not for $m = 10^{-22}$ eV.

In Fig. 2, we divide the power spectrum by the square of the linear growth factor $D(z)$ (where $D(z)$ is the CDM growth factor, which matches the FDM linear growth factor at low k). The normalization of $D(z)$ is chosen such that at $z = 100$, the ratio $\Delta^2(k, z)/D(z)^2$ is unity at the lowest comoving $k \sim 0.7$ h/Mpc. With this convention, the fact that on the left panel of Fig. 2, the power spectrum at all redshifts (solid lines) converges to unity at low k 's means the large length scale power is evolving correctly i.e. in accordance with linear perturbation theory expectation. The same is not true on the right panel, where the de Broglie scale is not resolved. The large length scale growth of the power spectrum is slower than it should be i.e. at low redshifts, the ratio $\Delta^2(k, z)/D(z)^2$ falls short of unity at low k 's (solid lines). This occurs despite the fact that those scales (say comoving $k \lesssim 1$ h/Mpc) are well resolved.

The Schrödinger-Poisson code thus behaves very differently from an N-body code or a fluid code. *For an N-body or fluid-formulation code, the correct evolution of power on some large scale requires only that large scale to be resolved. For a wave-formulation code, there is the additional requirement that the de Broglie scale be resolved, which is often more demanding.*

Also plotted in Fig. 2 are the results of a fluid-formulation solver that incorporates quantum pressure (dashed lines). One can see that the low k (large length scale) power spectrum evolves correctly in both cases i.e. a fluid solver is less demanding in terms of spatial resolution if one is only interested in large length scales. Note that the wave-formulation solver and the fluid-formulation solver differs in their predictions at high k 's (small length scales); the fluid solver predicts generally more power at high k 's. We interpret this as a by-product of the fluid code's failure to evolve correctly past regions of destructive interference (see Fig. 12 in Appendix A).

Fig. 3 shows a density slice of the wave-formulation simulation on the left and fluid-formulation simulation on the right (color coded for density) at $z = 5$, for the case of $m = 10^{-23}$ eV. One can see that the structures on large scales are broadly consistent. But the fluid simulation suffers from too much collapse and less wave-like structure on small scales, due to its inaccuracy in evolving past regions of destructive interference (see discussion

⁵ Both simulations use the *same* initial power spectrum [2] corresponding to an FDM mass of 10^{-22} eV.

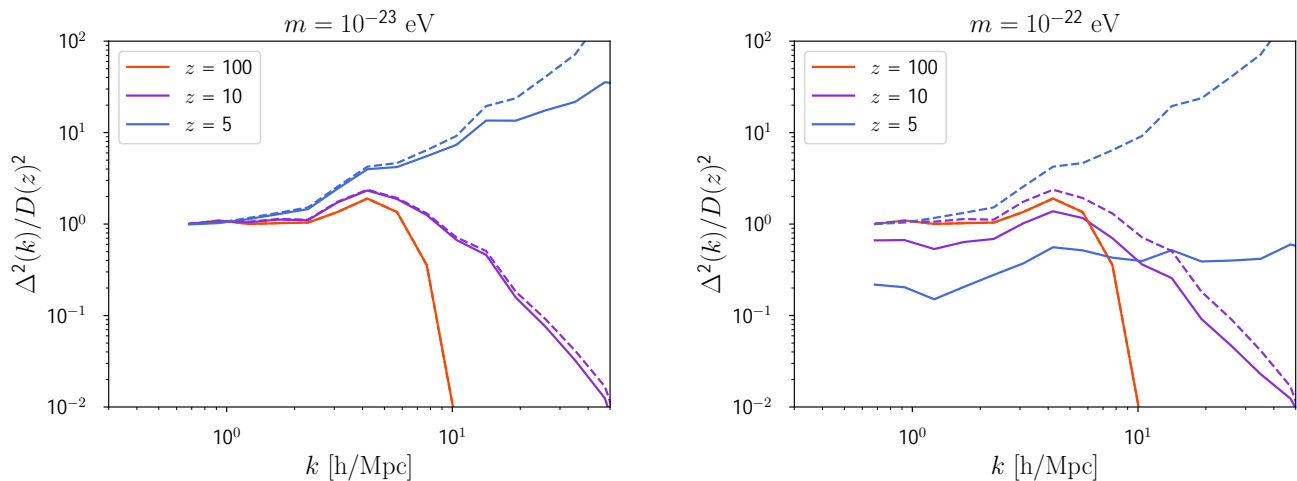


FIG. 2. Power spectrum evolution in a 10 Mpc/h box. Here, $\Delta^2(k, z) \equiv 4\pi P(k, z)/(2\pi)^3$ represents the dimensionless power. It is normalized by the linear growth factor $D(z)^2$ (according to CDM, which coincides with that for FDM at low k 's). The normalization of $D(z)$ is chosen such that the ratio $\Delta^2(k, z)/D(z)^2$ should be unity at low k 's if the power spectrum is evolving correctly. The solid lines represent the outputs from SPoS. The dashed lines represent the outputs from a fluid-Poisson solver that incorporates quantum pressure. *Left* – FDM (dynamics) mass $m = 10^{-23}$ eV. *Right* – FDM (dynamics) mass $m = 10^{-22}$ eV. The failure of the solid lines to converge to unity at low k 's for $z = 10$ and $z = 5$ is a sign that SPoS does not give the correct power spectrum evolution, because it is not resolving the de Broglie scale. On the other hand, the fluid-Poisson solver with quantum pressure gives the correct behavior at low k .

in Appendix A, around Fig. 12)– the density structure becomes inaccurate on small scales, which compromises also the computation of quantum pressure.

As a further test, we compare the predictions of third-order perturbation theory (specifically, the mass power spectrum including the one-loop corrections) with outputs from SPoS. The top panel of Fig. 4 shows the mass power spectrum for the case of an FDM mass of 10^{-23} eV, with a 10 Mpc/h comoving box and a 1024^3 grid.⁶ One can see that the one-loop power spectrum matches the numerical power spectrum up to a comoving $k \sim 3$ h/Mpc. We also show the numerical power spectrum with the same initial condition, box size and resolution, but with CDM dynamics (i.e. a pure N-body simulation with an initial power spectrum that corresponds to that of an FDM model). CDM dynamics appears to predict more power at high k 's compared to FDM dynamics.

The middle panel of Fig. 4 shows the same but with a 20 Mpc/h comoving box. One can see that the FDM numerical predictions fall short at low k because of the failure to resolve the de Broglie scale, while the CDM numerical predictions seem fine (at least at low k). The bottom panel of Fig. 4 shows the analog for an FDM mass of 10^{-22} eV. In this case, in order to resolve the de

Broglie scale, the box size has to be lowered to 3 Mpc/h comoving (the grid remains 1024^3). The lack of large scale power in the initial condition due to the small box size means the predicted matter power spectrum is lower than it should be. This should be kept in mind in applications of the code; we will return to this point below in the application to the Lyman-alpha forest.

IV. APPLICATION TO THE LYMAN-ALPHA FOREST

The Lyman-alpha forest consists of hydrogen absorption lines in the spectra of distant quasars. They provide useful constraints on the matter power spectrum at redshift $z = 2-6$ on scales down to about 0.1 Mpc comoving [28–32]. The small scale linear matter power spectrum is sensitive to assumptions about the nature of dark matter. For instance, warm dark matter causes a suppression of power on scales below its free-streaming scale, and can be constrained by the Lyman-alpha forest observations [33]. The warm dark matter constraint [33] can be roughly translated into a constraint on FDM which also suppresses power on small scales e.g. [8]. More recently, Lyman-alpha forest constraints on FDM were obtained by [23, 24], who simulated the FDM model using N-body simulations; the effect of “fuzziness” is accounted for purely through the initial conditions. In other words, the assumption was that CDM dynamics (with FDM initial condition) is sufficient to capture accurately the predictions of the FDM model. We are in a position to check this assumption, by comparing the outputs of an N-body

⁶ For Fig. 4, the initial condition uses an FDM mass that is consistent with the FDM dynamics i.e. 10^{-23} eV for the top and middle panel, and 10^{-22} eV for the bottom panel. In all cases, FDM predictions are computed with SPoS. The one-loop power spectrum is computed with an infra-red cut-off in the loop integral that corresponds to the box size in each case.

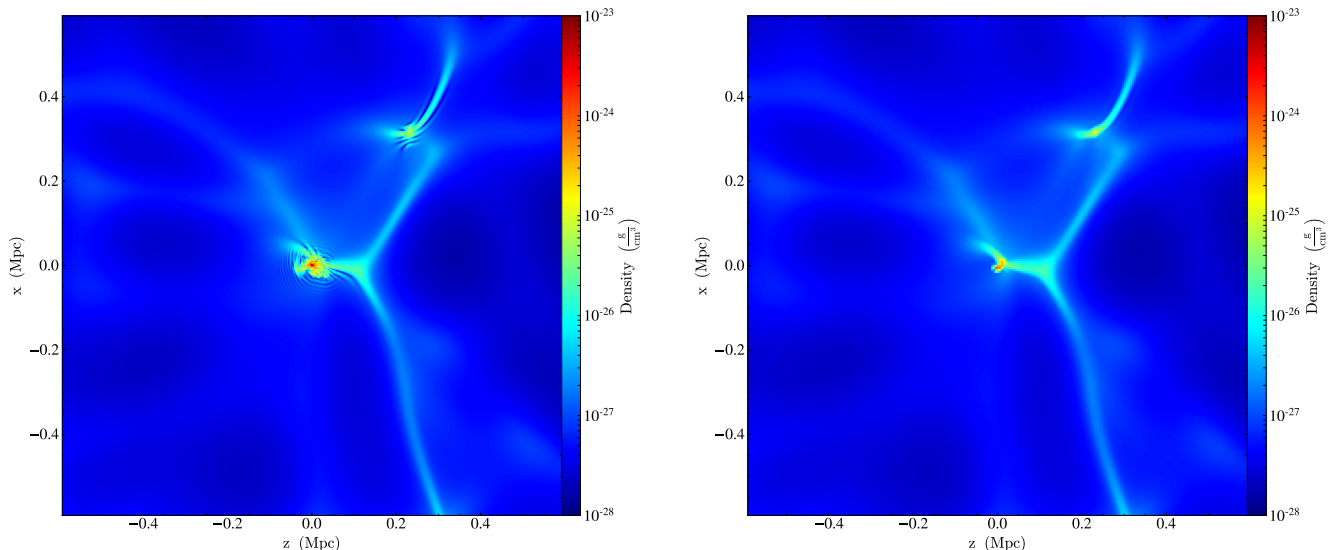


FIG. 3. A slice at $z = 5$ depicting density from simulations with $m = 10^{-23}$ eV (corresponding to Fig. 2). *Left* – wave-formulation simulation. *Right* – fluid-formulation simulation.

code (CDM dynamics) and SPoS (FDM dynamics), starting from the same initial condition. Let us stress that physical effects that cause additional sources of fluctuations, such as fluctuations in the ionizing background, are not addressed in this paper, even though they are probably important in assessing the reliability of the forest constraints on FDM or warm dark matter (see e.g. [8]).

A. The 1D Flux Power Spectrum - Methodology and Convergence Tests

The main observationally relevant quantity in the context of the Lyman-alpha forest is the one-dimensional (1D) flux power spectrum. The transmitted flux f is related to the optical depth τ by $f = e^{-\tau}$ (ignoring the continuum). The optical τ is strictly speaking an integral along the line of sight of the neutral hydrogen density field. Here, we employ a simple approximation (sometimes known as the local Gunn-Peterson approximation): $\tau = A(1 + \tilde{\delta})^2$ where A is a constant, and $\tilde{\delta}$ is a smoothed version of the overdensity δ i.e. in Fourier space:

$$\tilde{\delta}(k) = \exp \left[- \left(\frac{k}{k_f} \right)^2 \right] \delta(k) \quad (22)$$

where the smoothing is motivated by considerations of the effects of baryon pressure and the filtering scale is chosen to be $k_f = 40$ h/Mpc comoving [34].⁷ The constant A is determined by requiring that the mean flux $\langle f \rangle$

⁷ A number of quantities (such as the intergalactic medium temperature, which affects k_f , and the equation of state [35]) are im-

agree with the observed value at the redshifts of interest [33]. The three-dimensional (3D) flux power spectrum P_{3D}^f is computed in the usual way: by Fourier transforming the field f in the simulation box. The 1D flux power spectrum P^f is obtained by integrating P_{3D}^f :

$$P^f(k) = \int_k^\infty \frac{k' dk'}{2\pi} P_{3D}^f(k'). \quad (23)$$

We carry out a number of convergence tests to gauge the accuracy of our computation of $P^f(k)$ from the (Schrödinger-Poisson) simulations. We focus on results at $z = 5$, where most of the FDM constraints come from [23]. The left panel of Fig. 5 shows the ratio of $P^f(k)$ from two simulations with different resolution: one with a 512^3 grid and the other with a 1024^3 grid, both in a box of size 10 Mpc/h comoving. Each line represents the ratio P_{512}^f/P_{1024}^f with a different FDM mass.⁸ At low k 's, the two different resolutions give fairly close results, suggesting convergence. Even at $k \sim 0.1$ s/km (the highest

explicitly kept fixed in our simple model for τ . Varying them within observational bounds is not expected to significantly change our conclusions below.

⁸ In the test cases in this sub-section (IV A), the FDM mass refers to the FDM mass used in evolving the Schrödinger-Poisson system i.e. the dynamics mass. The initial conditions were chosen to be identical i.e. the initial power spectrum corresponds to that of an FDM mass of 10^{-22} eV. By doing this, we perform tests more stringently with more initial small scale fluctuations in the computational box. Otherwise if initial conditions consistent with small dynamical FDM mass are used, the initial small scale power will be more suppressed. We expect the small scale overdensity to stay longer in the stage of linear growth, and the results to be better than our test simulations.

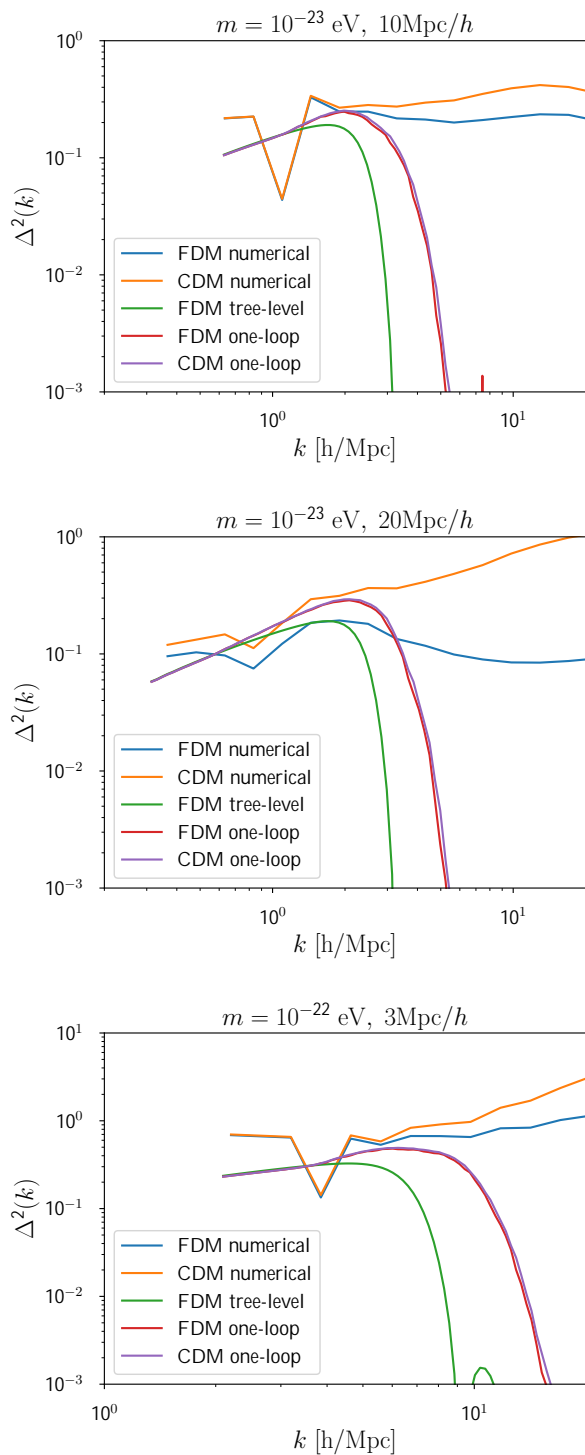


FIG. 4. Comparison of mass power spectrum between simulations and perturbative calculations. The top (orange) line is from an N-body simulation i.e. CDM dynamics but from the same initial condition. The next lower (blue) line is from SPoS. The next two lines (red and purple) are the one-loop predictions from FDM and CDM dynamics respectively. The lowest (green) line is the linear (tree) FDM power spectrum. *Top* – FDM mass 10^{-23} eV in a 10 Mpc/h box. *Middle* – FDM mass 10^{-23} eV in a 20 Mpc/h box. *Bottom* – FDM mass 10^{-22} eV in a 3 Mpc/h box.

k accessible in the relevant data [23]), we see that as long as the FDM mass is below $\sim 2 \times 10^{-23}$ eV, the 1024^3 grid simulation (in a 10 Mpc/h box i.e. a resolution of about 0.01 Mpc/h comoving) should give results accurate at the 5% level or better.

Since our interest is mainly in exploring the difference in implications between FDM and CDM dynamics, we show in the right panel of Fig. 5 another version of the resolution convergence test. Plotted in the figure is the ratio P_{CDM}^f (from N-body simulations i.e. CDM dynamics) to P_{FDM}^f (from Schrödinger-Poisson simulations i.e. FDM dynamics), starting from the same initial condition in a 10 Mpc/h box. The solid and dashed lines represent the results from simulations with a 1024^3 grid and a 512^3 grid respectively. It appears P_{CDM}^f/P_{FDM}^f is accurate at the few percent level, for $k \lesssim 0.1$ s/km, as long as the FDM mass is less than $\sim 2 \times 10^{-23}$ eV and the resolution is about 0.01 Mpc/h comoving (roughly that of a 1024^3 grid in a 10 Mpc/h box).

It is worth noting that even though the CDM and FDM dynamics are identical on large scales, and thus the predicted mass power spectrum agrees between the two (see Sec. III), the flux power spectrum P^f does not agree between the two on large scales (low k 's). There are two reasons for this: (1) the very nonlinear transformation from density to flux mixes scales, and (2) the 1D flux power spectrum P^f is itself an integral of the 3D flux power spectrum that receives contributions from high k 's (see Eqn. 23). If the ratio P_{CDM}^f/P_{FDM}^f were scale independent, then the fact that the ratio differs from unity is not so important, since there are free parameters, such as σ_8 and A or the level of the ionizing background, that can be adjusted in the Lyman-alpha forest model to produce roughly the same effect (i.e. moving P^f up and down). From the right panel of Fig. 5, we see that this ratio is dependent on k —indeed it rises with increasing k —and it is important to ensure it does not become too large if one were to use N-body dynamics to approximate FDM dynamics, as is commonly done.

The effect of a finite box size is shown in Fig. 6. On the left panel, we compare the flux power spectrum from simulations with different box sizes: P_{10Mpc}^f from a 10 Mpc/h box and P_{20Mpc}^f from a 20 Mpc/h box. The resolution is kept fixed: a 512^3 grid is employed for the 10 Mpc/h simulations while a 1024^3 grid is used for the 20 Mpc/h simulations. We see that P_{20Mpc}^f and P_{10Mpc}^f differ by more than 10% across a wide range of scales, suggesting non-negligible box size effects; in other words, a 10 Mpc/h box is too small to reliably predict the flux power spectrum. It might thus seem impossible to satisfy the twin demands of high resolution and large box size, given that the largest grid we can practically simulate is about 1024^3 .

Fortunately, for the present purpose, what we care about is the difference between CDM and FDM dynamics, exemplified in the ratio P_{CDM}^f/P_{FDM}^f . This is shown on the right panel of Fig. 6. We see that the different

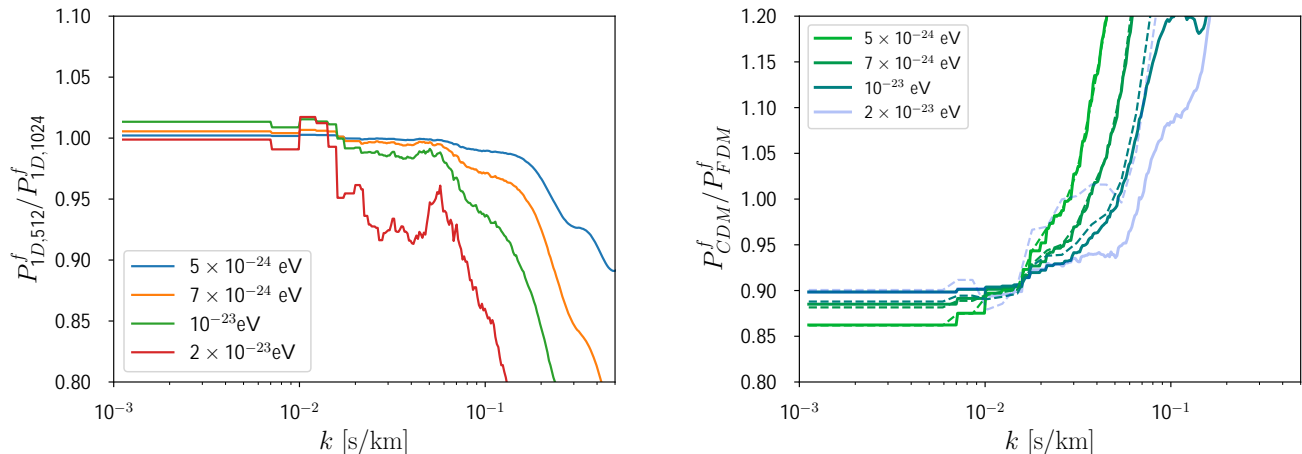


FIG. 5. Convergence test of 1D flux power spectrum at $z = 5$ in a comoving box of 10 Mpc/h. *Left* – Ratio of the 1D flux spectrum P^f at $z = 5$ from Schrödinger-Poisson simulations with a 512^3 grid to P^f from simulations with a 1024^3 grid, for various FDM dynamics masses. *Right* – The 1D flux spectrum P^f with CDM dynamics divided by P^f with FDM dynamics, for different resolutions and various FDM masses. Solid and dashed lines represent the resolution of a 1024^3 grid and a 512^3 grid respectively.

box sizes (solid lines for a 10 Mpc/h box, dashed lines for a 20 Mpc/h box) give fairly similar results for this ratio, as long as the FDM mass is small enough i.e. the de Broglie scale is resolved – the case of 2×10^{-23} eV is one where the de Broglie scale is *not* resolved, as we already know from the resolution tests discussed earlier (i.e. a grid of 1024^3 is inadequate for a box as big as 20 Mpc/h).

Henceforth, for a given FDM mass, we choose a box size small enough so that a 1024^3 -grid simulation can resolve the de Broglie wavelength. This in general means the flux power spectrum P^f has large finite-box corrections. However, since such corrections affect the CDM-dynamics and FDM-dynamics simulations in similar ways, the ratio P^f_{CDM}/P^f_{FDM} is actually reliable and sufficiently accurate for our purpose.

B. The 1D Flux Power Spectrum – CDM versus FDM Dynamics

Adopting the methodology laid out above, we carry out a series of simulations of different FDM masses where the de Broglie scale is resolved (by adjusting the box size and always using a 1024^3 grid). Here, the initial power spectrum has the same FDM mass as that used in the dynamics. Our aim is to determine the scales at $z = 5$ where P^f_{CDM} from N-body simulations can be used to approximate P^f_{FDM} from FDM dynamics, as a function of FDM mass. We run simulations with FDM masses ranging from 10^{-23} eV to 10^{-22} eV and adjust the box size by requiring that the large scale matter power spectrum follows the linear evolution. By doing this, we can make sure the de Broglie wavelength is resolved, otherwise the

evolution of large scale mass power spectrum will deviate from the linear evolution as demonstrated in Sec. III B.

Fig.7 shows the ratio of P^f_{CDM}/P^f_{FDM} with each line representing a different FDM mass. The ratio follows the same trend as the test simulations: on large scales, P^f from CDM and FDM dynamics are close to each other (differ less than 10%) and on small scales, P^f_{CDM} overestimates P^f_{FDM} . The scale k at $z = 5$ where P^f_{CDM} starts to overestimate P^f_{FDM} moves to smaller scales with increasing FDM mass.⁹ To quantify this effect, we define k_d to be the smallest k where P^f_{CDM} exceeds P^f_{FDM} by 10%. Fig.8 shows the relation between the scale k_d as a function of FDM mass. Black triangles are the numerical data which closely follow a power law relation given by the blue line

$$k_d \approx 0.23 \text{ s/km} \left(\frac{m}{10^{-22} \text{ eV}} \right)^{0.56}. \quad (24)$$

For general FDM masses, we can read from the power law relation the scales where P^f_{CDM} from N-body simulations is a good approximation of P^f_{FDM} at $z = 5$. For example, for FDM masses larger than 2×10^{-23} eV, P^f_{CDM} differs from P^f_{FDM} by less than 10% on our current observational scale of Lyman-alpha forest $k \lesssim 0.1$ s/km [28–32]. Therefore, one can avoid running expensive large scale FDM simulations where the small de Broglie wave-

⁹ The fact that P^f_{CMD} and P^f_{FDM} have smaller deviations on large scales than the test simulations is consistent with what we discussed before. Fewer initial small scale fluctuations leave the system longer in the linear growth stage and yield better agreement.

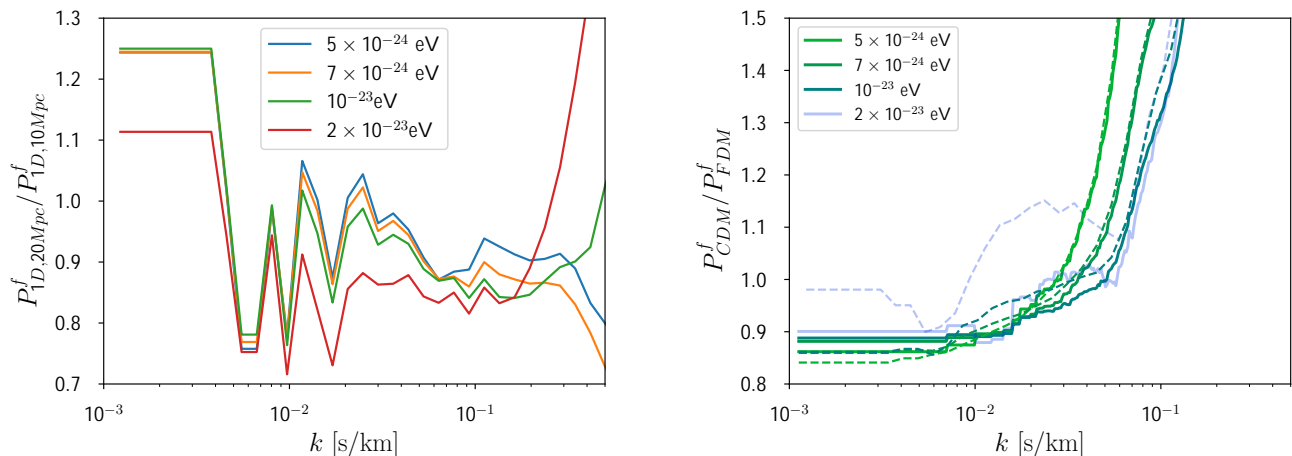


FIG. 6. Test of finite box size correction of the 1D flux power spectrum at $z = 5$. *Left* – Ratio of P^f from simulations with a box size of 10 Mpc/h to P^f from simulations with a size of 20 Mpc/h, for various FDM masses, keeping the resolution fixed. *Right* – The 1D flux spectrum P^f with CDM dynamics divided by P^f with FDM dynamics, for different box sizes and various FDM masses. Solid and dashed lines represent a box size of 10 Mpc/h and 20 Mpc/h respectively.

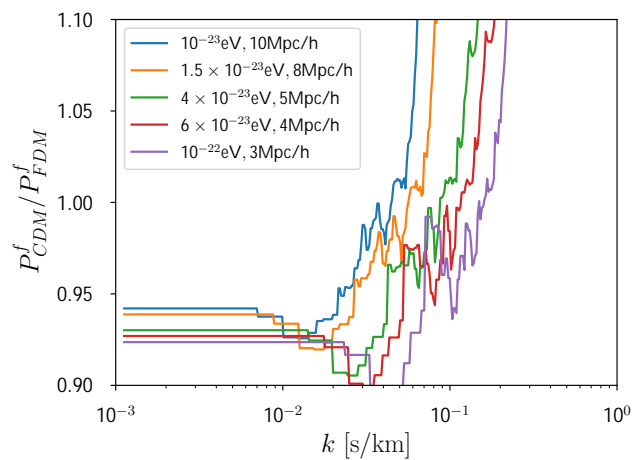


FIG. 7. The 1D flux spectrum P^f at $z = 5$ with CDM dynamics divided by P^f with FDM dynamics for realistic simulation with consistent FDM mass in the initial condition and the dynamics. Each line represents a simulation with different FDM mass and box size adjusted to resolve the de Broglie wavelength.

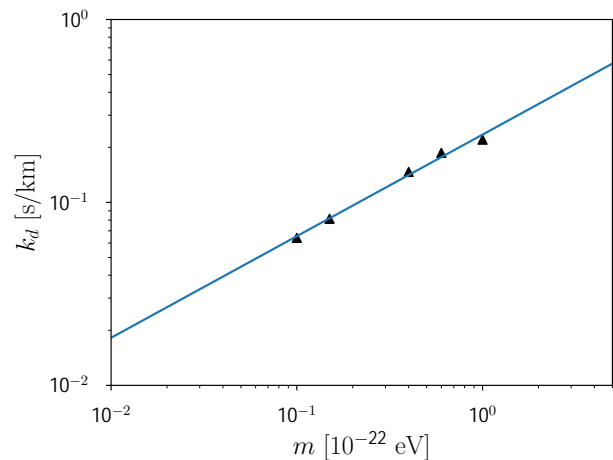


FIG. 8. Relation between k_d and FDM masses. The best fit line follows $k_d = 0.23 \text{ s/km} (m/10^{-22} \text{ eV})^{0.56}$.

length has to be resolved, but perform relatively cheap N-body simulations to obtain good approximation of P_{FDM}^f and compare with observations. It is worth emphasizing though that for other applications, such as investigating galactic sub-structure, correctly simulating the FDM dynamics is crucial (see discussion in Sec. III B).

V. DISCUSSION

In this paper, we present numerical and perturbative computations of the FDM model.

Perturbative calculations are carried out for both the fluid and wave formulations. For fluid perturbation theory, this is done up to third order, focusing in particular on the one-loop mass power spectrum (Appendix B). Wave perturbation theory (Appendix C) has a more limited regime of validity compared to fluid perturbation theory; namely the former requires the physical length scale of interest be smaller than the de Broglie wavelength (Eqn. (C7)) i.e. simply requiring small density fluctuation δ is not sufficient. Wave perturbation theory thus

breaks down rather early in cosmic history, even when fluid perturbation theory is safely in the linear regime. The wave description might still be useful for analytic understanding in the highly nonlinear regime, especially in the context of complex interference structures—a subject we hope to return in the future.

On the numerical side, we perform cosmological simulations of FDM using both a Schrödinger-Poisson solver and a fluid solver. The fluid solver integrates the Madelung formulation of the Schrödinger equation and is able to produce the correct structures on large scales. However, small scale oscillatory features (from wave interference) observed in the Schrödinger-Poisson simulations are not reproduced by the fluid simulations. In particular, the fluid solver fails to simulate the correct dynamics when the local density vanishes due to the destructive interference of waves, as demonstrated in Appendix A 3. This is understandable because the quantum pressure in the fluid formulation becomes ill-defined where the fluid density vanishes (Eqn. (9)). The failure of the fluid solver to give the correct quantum pressure in regions of complex interference results in artificially enhanced gravitational collapse, and over-predicts the mass power spectrum on small scales. Whether Lagrangian fluid codes like the SPH method [18] suffer from the same problem is not clear, and we recommend similar tests to those in Appendix A 3 be carried out.

Our Schrödinger-Poisson solver SPoS, on the other hand, is able to simulate the correct dynamics on small scales. We obtain good agreement with third order perturbative calculations up to the mildly nonlinear scale. However, SPoS is demanding in resolution in that it requires the (typically small) de Broglie wavelength to be resolved, even if one is primarily interested in structures on much larger scales.

As an application, we compare the 1D Lyman-alpha flux power spectrum P_{CDM}^f from N-body simulations with that computed from FDM dynamics, P_{FDM}^f , using the same FDM initial conditions and determine the scales where P_{CDM}^f is a good approximation to P_{FDM}^f . Though P^f from both CDM and FDM dynamics suffer from non-negligible finite box corrections, we find the ratio P_{CDM}^f/P_{FDM}^f is reliable and independent of box size as long as the de Broglie wavelength is resolved. The ratio P_{CDM}^f/P_{FDM}^f is close to unity on large scales with deviation less than 10%, but it eventually grows much larger on small scales. We quantify the scales of agreement between the two flux power spectra by measuring the smallest k_d (largest length scale) where $P_{CDM}^f/P_{FDM}^f > 1.1$, and our results suggest k_d increases with FDM mass as $k_d \propto m^{0.56}$. For FDM masses larger than 2×10^{-23} eV, $k_d > 0.1$ s/km, therefore P_{CDM}^f is a good approximation to P_{FDM}^f on our current observational scales of the Lyman-alpha forest $\lesssim 0.1$ s/km [28–32].

There have been a number of efforts to constrain FDM properties using Lyman-alpha forest observations, including [23] using XQ-100 and HIRES/MIKE data, and

[24] using SDSS data. Both groups employed N-body simulations with initial conditions modified by FDM and use P_{CDM}^f to approximate P_{FDM}^f . Our results confirm the validity of their approximation. However, a number of astrophysical effects likely play a role in interpreting the Lyman-alpha forest data, such as the spatial fluctuations of the ionizing background and temperature at high redshifts, and galactic winds at low redshifts. It is unclear if current attempts to model these effects faithfully capture the range of possibilities (e.g. see discussion in [8]). More work remains to be done in this direction.

Appendix A: FDM with a Fluid Solver

Our fluid solver for FDM dynamics is implemented in the ENZO code [26] by modifying the built-in 3D Zeus code [36, 37] to incorporate the quantum pressure. The built-in Zeus method is an explicit method that solves the fluid transport on a Cartesian grid using an operator-split scheme. The whole method contains two steps: *source* and *transport*. In the source step, only velocities are updated due to the gravitational acceleration (and, in the non-FDM implementation, the pressure gradient terms). Artificial viscosity, which is used in the original fluid solver to smooth shock fronts, is not needed for FDM dynamics, as the quantum pressure strongly disfavors sharp gradients. In the transport step, the mass and momentum fluxes are constructed and used to update the density and velocity through the conservative form of the fluid equations.

The quantum pressure term for FDM is included in the source step as an extra term for the acceleration. The quantum pressure $p = -\frac{1}{2}\nabla^2 \log \rho - \frac{1}{4}(\nabla \log \rho)^2$ is computed with a 4th-order accurate finite difference method. Apart from the existing time step constraints already in ENZO, the time step must also respects the CFL condition for parabolic systems: $\Delta t \leq (\Delta x)^2 m a^2 / (6\hbar)$.

Below we describe a number of one-dimensional tests. All the tests are performed without gravity and cosmological expansion (i.e. $a = 1$).

One obvious worry is that the quantum pressure becomes ill-defined when ρ vanishes. Of course, numerically, the density ρ never vanishes exactly (nor does it go negative in all cases we check); the question is whether the large quantum pressure associated with regions of low density leads to unacceptable inaccuracies (see Test 3 below).

1. A Test with a Gaussian Density Profile

The evolution of a Gaussian wave packet admits a simple analytical solution for the 1D free Schrödinger equation without an external potential:

$$\psi(t, x) = \sqrt{\frac{1}{\alpha + i\frac{\hbar t}{m}}} \exp\left(-\frac{x^2}{2(\alpha + i\frac{\hbar t}{m})}\right), \quad (\text{A1})$$

where α is a constant and can be set to be real for simplicity. The density and velocity follow from the wave function as

$$\rho = \frac{1}{\sqrt{\alpha^2 + \frac{\hbar^2 t^2}{m^2}}} \exp\left(-\frac{\alpha x^2}{\alpha^2 + \frac{\hbar^2 t^2}{m^2}}\right), \quad (\text{A2})$$

$$v = \frac{x}{\alpha^2 + \frac{\hbar^2 t^2}{m^2}} \frac{\hbar^2 t}{m^2}. \quad (\text{A3})$$

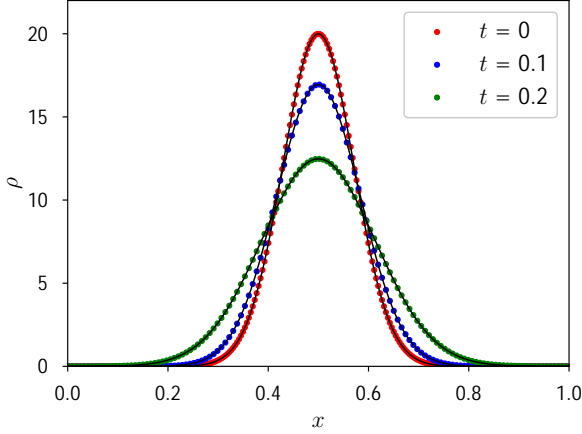


FIG. 9. Comparison of analytical and numerical results for the density evolution of a Gaussian wave packet. Solid lines represent the exact solutions while dots represent the numerical results from a fluid simulation. The times shown are from top to bottom $t = 0, 0.1, 0.2$ in code units (see text).

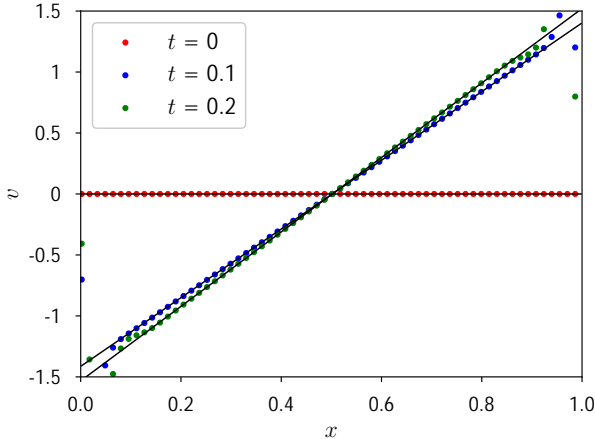


FIG. 10. Comparison of analytical and numerical results for the velocity evolution of a Gaussian wave packet. Solid lines represent the exact solutions and dots represent the numerical results from a fluid simulation. The flat line corresponds to $t = 0$. Of the tilted lines, the steeper one corresponds to $t = 0.2$ while the other is at $t = 0.1$.

Fig.(9) and (10) show the comparison between analytical solutions and numerical results (using the modified ENZO fluid code). We start at $t = 0$ where $v = 0$ in the simulation box. The parameters are chosen to be $\alpha = 1/100$ and $\hbar/m = 0.0626$ in the code's internal unit system. Solid lines represent analytical solutions and colored dots are numerical results at different time. We can see the numerical values follow closely to the analytical solutions. The discrepancies of velocity near the boundaries are due to the periodic boundary condition we use for our finite box size.

2. A Test with a Density Jump

One might worry that the fluid solver could miss non-trivial wave interference effects. Here we demonstrate that the quantum pressure term, when properly incorporated in a fluid code, is capable of reproducing intricate interference patterns expected in certain solutions. In particular, let us focus on a self-similar solution of the free Schrödinger equation [8]:

$$\psi(t, x) = \frac{\mathcal{A}}{2} + \mathcal{B} - \frac{\mathcal{A}}{2}(1 \mp i)\mathcal{C}\left(x\sqrt{\frac{m}{\pi\hbar|t|}}\right) - \frac{\mathcal{A}}{2}(1 \pm i)\mathcal{S}\left(x\sqrt{\frac{m}{\pi\hbar|t|}}\right), \quad (\text{A4})$$

where the upper/lower sign is for a positive/negative t and \mathcal{A}, \mathcal{B} are constants. The functions \mathcal{C} and \mathcal{S} are the Fresnel integrals

$$\mathcal{C}(\theta) = \int_0^\theta \cos\left(\frac{\pi\xi^2}{2}\right)d\xi, \quad (\text{A5})$$

$$\mathcal{S}(\theta) = \int_0^\theta \sin\left(\frac{\pi\xi^2}{2}\right)d\xi. \quad (\text{A6})$$

The density profile $\rho = |\psi|^2$ given by this solution asymptotes to $(\mathcal{A} + \mathcal{B})^2$ as $x \rightarrow -\infty$ and \mathcal{B}^2 as $x \rightarrow \infty$. At $t = 0$, the density profile becomes a step function with constant value $(\mathcal{A} + \mathcal{B})^2$ and \mathcal{B}^2 for $x < 0$ and $x > 0$. There is a singularity at $x = 0$, where a sharp density jump exists, while the velocity remains regular and is zero everywhere.

The analytical evolution of the solution can be understood through the Fourier transform of the wave function. The initial step function of density profile contains the waves of all wavelengths with the dispersion relation derived by the Schrödinger equation $\omega \propto k^2$. Those waves do not couple with each other and evolve independently. Waves with short wavelength have larger speed but smaller amplitude. They propagate faster and leave the longer wave modes behind, leading to an intricate interference pattern.

Fig.(11) presents snapshots of the density evolution starting from a step-function at $t = 0$. The constants are chosen such that $\hbar/m = 0.0626$, $\mathcal{B} = \sqrt{6}$ and $\mathcal{A} = \sqrt{5} - \sqrt{6}$, so the initial density has value 6 and

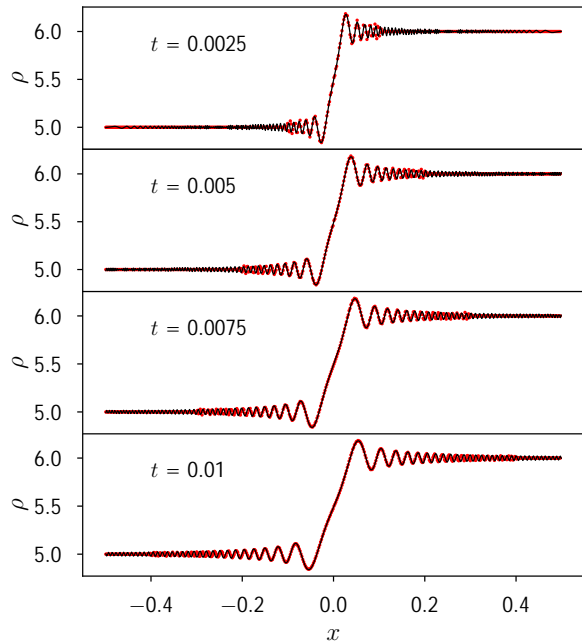


FIG. 11. Snapshots of density evolution from the density jump. Solid (black) lines represent the exact solutions. The (red) dots represent numerical results from a fluid simulation.

5 on the right and left side of the origin. The initial density jump at the origin launches waves which propagate away from it. At the front of the wave propagation, the wavelength and amplitude of oscillations are getting smaller. The numerical results agree well with the analytical results, as long as the relevant oscillations are resolved.

3. A Failed Test: Collision of Two Wave Packets

A particular demanding test of the fluid formulation is to investigate a case where the density vanishes in isolated places. The quantum pressure p becomes ill-defined and the fluid solver might not yield the correct evolution. On the other hand, one might hope that inaccuracies at isolated points do not affect significantly the overall global evolution. This turns out not to be the case in this example.

The free Schrödinger equation admits a solution where a single Gaussian wave packet moves with momentum $\hbar k$

$$\psi(x, t) = \sqrt{\frac{\alpha}{\alpha + i\frac{\hbar}{m}t}} \exp\left[-\frac{(x + x_0 - ik\alpha)^2}{2(\alpha + i\frac{\hbar}{m}t)}\right] \exp\left(-\frac{\alpha k^2}{2}\right) \quad (\text{A7})$$

The linearity of the Schrödinger equation allows two meeting wave packets to evolve on their own and pass

through each other, for instance:

$$\psi(x, t) = \sqrt{\frac{\alpha}{\alpha + i\frac{\hbar}{m}t}} \exp\left[-\frac{(x + x_0 - ik\alpha)^2}{2(\alpha + i\frac{\hbar}{m}t)}\right] \exp\left(-\frac{\alpha k^2}{2}\right) + \sqrt{\frac{\alpha}{\alpha + i\frac{\hbar}{m}t}} \exp\left[-\frac{(x - x_0 + ik\alpha)^2}{2(\alpha + i\frac{\hbar}{m}t)}\right] \exp\left(-\frac{\alpha k^2}{2}\right). \quad (\text{A8})$$

The density and velocity can be deduced in this situation

$$\rho = m|\psi|^2, \quad v = \frac{\hbar}{2im} \frac{\psi^* \nabla \psi - \psi \nabla \psi^*}{\rho}. \quad (\text{A9})$$

Fig.12 shows the comparison between the analytical and numerical solutions (using the fluid code). In this numerical test, we take $\alpha = 1/500$, $k = 20\pi$ and $x_0 = 0.1$. As the two wave packets move towards each other, at some point the interference between two waves results in vanishing density in certain locations. In the snapshots, the numerical solution follows the analytical evolution very well until the vanishing density region from interference first appears (middle panel). After that, the numerical solution deviates from the analytical solution.

The local densities at the position of destructive interference in the fluid code are very small, but remain positive and never reach zero. The error of density in those regions can not be smaller than machine error which effectively acts as a density floor. On the other hand, the true quantum pressure (Eqn. 9) is proportional $\log \rho$ and diverges at the region of destructive interference diverges. However small the error of the local density is, the error of the quantum pressure is always infinite where the true density is zero. Therefore, the simulated dynamics deviates from the analytical solution after the destructive interference shows up. We have verified that this result is independent of the spatial or temporal resolution employed.

Where the density is very low in the numerical simulations, the quantum pressure is large and susceptible to sizable numerical errors. The velocity suffers from a similar problem. One might think evolving the momentum density (as opposed to velocity) could alleviate this problem. This is partly true: the momentum density in fact vanishes in these places where the density vanishes. The issue is that one still needs to advect the momentum density by a suitable velocity field: the ill-defined nature of the velocity (or its very large value) in such locations remains a problem.

Destructive interference like that depicted in Fig. 12 might seem like a rather artificial situation, but it turns out to be a fairly generic occurrence in the nonlinear regime (see discussion in Sec. III). The fact that the fluid code fails to evolve correctly past regions of destructive interference cause it to over-predict the amount of power on small scales (see Fig. 2 and 3 in Sec. III). One can circumvent this problem by switching to a wave code, or by developing some kind of a hybrid code (fluid on large scales, wave on small scales) which could combine the best features of both formulations. We have checked

that the wave code successfully evolves past these regions of vanishing density (a plot of the numerical solution against the analytical one would not be too instructive, as they lie on top of each other).

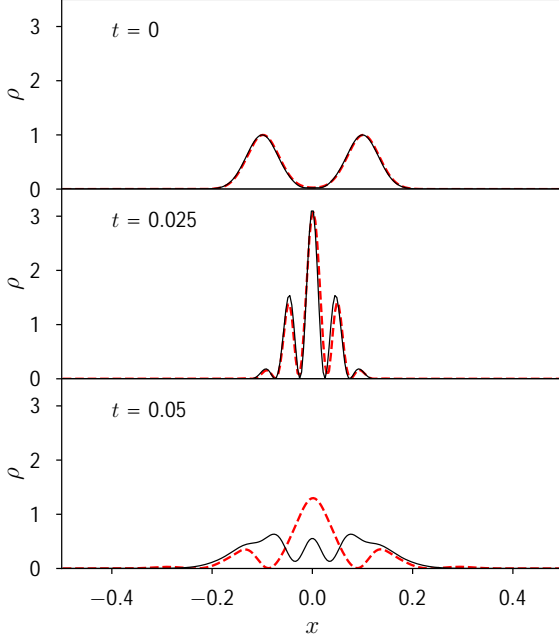


FIG. 12. Snapshots of density evolution for the collision of two Gaussian wave packets. Solid (black) lines represent the exact solution. Dashed (red) lines represent the numerical results from a fluid simulation. A wave simulation, on the other hand, reproduces the exact solution very closely; the wave simulation results essentially lie on top of the solid (black) lines.

Appendix B: Fluid Perturbation Theory

The fluid formulation of the dynamics takes the form:

$$\partial_\eta \delta + \nabla_i [(1 + \delta)v^i] = 0, \quad (\text{B1})$$

$$\partial_\eta v^i + \frac{\partial_\eta a}{a} v^i + v^j \nabla_j v^i = -\nabla_i \Phi + \frac{1}{2\bar{m}^2 a^2} \nabla_i \frac{\nabla^2 \sqrt{1 + \delta}}{\sqrt{1 + \delta}}, \quad (\text{B2})$$

$$\nabla^2 \Phi = 4\pi G a^2 \bar{\rho} \delta, \quad (\text{B3})$$

where δ is the overdensity defined by $\rho \equiv \bar{\rho}(1 + \delta)$, with $\bar{\rho}$ being the mean density. Here ∂_η denotes derivative with respect to conformal time η . The conformal time η is related to proper time t by $a d\eta = dt$, where a is the scale factor. We introduce the symbol $\bar{m} \equiv m/\hbar$ to

suppress factors of \hbar . The last term of Eqn. (B2) is often referred to as quantum pressure, though it strictly speaking arises from a stress tensor that has off-diagonal terms.

Assuming gradient flow, defining $\Theta \equiv \nabla_i v^i$ and using $\delta(\mathbf{k})$ to denote the Fourier transform of $\delta(\mathbf{x})$ i.e.

$$\delta(\mathbf{x}) = \int \frac{d^3 k}{(2\pi)^3} \delta(\mathbf{k}) e^{i\mathbf{k}\cdot\mathbf{x}} \quad (\text{B4})$$

Following standard perturbation theory techniques (e.g. [38–42]), the fluid equations can be rewritten as

$$\partial_\eta \delta(\mathbf{k}) + \Theta(\mathbf{k}) = - \int \frac{d^3 k_1 d^3 k_2}{(2\pi)^3} \delta_D(\mathbf{k} - \mathbf{k}_{12}) \frac{\mathbf{k} \cdot \mathbf{k}_2}{k_2^2} \delta(\mathbf{k}_1) \Theta(\mathbf{k}_2), \quad (\text{B5})$$

$$\begin{aligned} \partial_\eta \Theta(\mathbf{k}) + \frac{\partial_\eta a}{a} \Theta(\mathbf{k}) + 4\pi G a^2 \bar{\rho} \delta(\mathbf{k}) - \frac{k^4}{4a^2 \bar{m}^2} \delta(\mathbf{k}) = \\ - \int \frac{d^3 k_1 d^3 k_2}{(2\pi)^3} \delta_D(\mathbf{k} - \mathbf{k}_{12}) \left[\frac{1}{2} k^2 \frac{\mathbf{k}_1 \cdot \mathbf{k}_2}{k_1^2 k_2^2} \Theta(\mathbf{k}_1) \Theta(\mathbf{k}_2) \right. \\ \left. + \frac{k^4}{16a^2 \bar{m}^2} \left(1 + \frac{k_1^2 + k_2^2}{k^2} \right) \delta(\mathbf{k}_1) \delta(\mathbf{k}_2) \right] \\ + \int \frac{d^3 k_1 d^3 k_2 d^3 k_3}{(2\pi)^6} \delta_D(\mathbf{k} - \mathbf{k}_{123}) \delta(\mathbf{k}_1) \delta(\mathbf{k}_2) \delta(\mathbf{k}_3) \frac{k^4}{32a^2 \bar{m}^2} \\ \left[1 + \frac{k_1^2 + k_2^2 + k_3^2}{k^2} + \frac{k_{12}^2 + k_{23}^2 + k_{31}^2}{3k^2} \right] \\ + \dots, \end{aligned} \quad (\text{B6})$$

where the symbols \mathbf{k}_{12} and \mathbf{k}_{123} denote respectively $\mathbf{k}_1 + \mathbf{k}_2$ and $\mathbf{k}_1 + \mathbf{k}_2 + \mathbf{k}_3$. The symbol δ_D represents the Dirac delta function. The ellipsis on the right hand side of Eqn. (B6) represents higher order terms $O(\delta^4)$.

For simplicity, we consider a matter-dominated flat universe (a very good approximation at redshift $1000 > z > 1$) i.e. $a = \bar{H}_0^2 \eta^2 / 4$. Here, \bar{H}_0 is an effective Hubble constant, and is related to the actual Hubble constant H_0 by $\bar{H}_0 = H_0 \Omega_{m0}^{1/2}$ (where Ω_{m0} is the matter density today). It is helpful to define $\bar{\eta} \equiv \bar{H}_0 \eta$ and $\bar{\Theta} \equiv \Theta / \bar{H}_0$, and rewrite the equations as:

$$\begin{aligned} \partial_{\bar{\eta}} \Psi_a(\mathbf{k}) + \Omega_{ab}(\mathbf{k}) \Psi_b(\mathbf{k}) = \\ \int \frac{d^3 k_1 d^3 k_2}{(2\pi)^3} \delta_D(\mathbf{k} - \mathbf{k}_{12}) \gamma_{abc}(\mathbf{k}, \mathbf{k}_1, \mathbf{k}_2) \Psi_b(\mathbf{k}_1) \Psi_c(\mathbf{k}_2) \\ + \int \frac{d^3 k_1 d^3 k_2 d^3 k_3}{(2\pi)^6} \delta_D(\mathbf{k} - \mathbf{k}_{123}) \Gamma_{abcd}(\mathbf{k}, \mathbf{k}_1, \mathbf{k}_2, \mathbf{k}_3) \\ \Psi_b(\mathbf{k}_1) \Psi_c(\mathbf{k}_2) \Psi_d(\mathbf{k}_3) \\ + \dots \end{aligned} \quad (\text{B7})$$

where repeated indices e.g. b, c are implicitly summed, and all quantities are functions of time $\bar{\eta}$. The two-component vector Ψ represents:

$$\begin{bmatrix} \Psi_1 \\ \Psi_2 \end{bmatrix} \equiv \begin{bmatrix} \delta \\ \bar{\Theta} \end{bmatrix}. \quad (\text{B8})$$

The matrix $\Omega(\mathbf{k})$ represents:

$$\begin{bmatrix} \Omega_{11} & \Omega_{12} \\ \Omega_{21} & \Omega_{22} \end{bmatrix} \equiv \begin{bmatrix} 0 & 1 \\ \frac{6}{\bar{\eta}^2} - \frac{b_k^2}{\bar{\eta}^4} & \frac{2}{\bar{\eta}} \end{bmatrix}, \quad (\text{B9})$$

where

$$b_k \equiv \frac{2k^2}{\bar{m}\bar{H}_0}. \quad (\text{B10})$$

The matrix $\gamma_{abc}(\mathbf{k}, \mathbf{k}_1, \mathbf{k}_2)$ is defined by:

$$\begin{bmatrix} \gamma_{111} & \gamma_{112} \\ \gamma_{121} & \gamma_{122} \end{bmatrix} \equiv - \begin{bmatrix} 0 & \frac{\mathbf{k}\cdot\mathbf{k}_2}{2k_2^2} \\ \frac{\mathbf{k}\cdot\mathbf{k}_1}{2k_1^2} & 0 \end{bmatrix}, \quad (\text{B11})$$

$$\begin{bmatrix} \gamma_{211} & \gamma_{212} \\ \gamma_{221} & \gamma_{222} \end{bmatrix} \equiv - \begin{bmatrix} \frac{b_k^2}{4\bar{\eta}^4} \left(1 + \frac{k_1^2 + k_2^2}{k^2}\right) & 0 \\ 0 & \frac{k^2 \mathbf{k}_1 \cdot \mathbf{k}_2}{2k_1^2 k_2^2} \end{bmatrix}, \quad (\text{B12})$$

and all components of $\Gamma_{abcd}(\mathbf{k}, \mathbf{k}_1, \mathbf{k}_2, \mathbf{k}_3)$ vanish except for:

$$\Gamma_{2111} \equiv \frac{b_k^2}{8\bar{\eta}^4} \left(1 + \frac{k_1^2 + k_2^2 + k_3^2}{k^2} + \frac{k_{12}^2 + k_{23}^2 + k_{31}^2}{3k^2}\right) \quad (\text{B13})$$

Examining Eqn. (B6), the scale k at which the last two terms on the left balance each other can be thought of as the Jeans scale i.e. when $b_k^2 = 6\bar{\eta}^2$:

$$k_{\text{Jeans}} = \frac{44.7}{\text{Mpc}} \left(6a \frac{\Omega_{m0}}{0.3}\right)^{1/4} \left(\frac{H_0}{70 \text{ km/s}} \frac{m}{10^{-22} \text{ eV}}\right)^{1/2}. \quad (\text{B14})$$

The quantum pressure becomes important at $k > k_{\text{Jeans}}$. We stress that the Jeans scale is a linear perturbation theory concept. In fact, it is worth briefly commenting on how the quantum pressure behaves beyond linear theory. For a qualitative understanding, it's helpful to revert back to position space in which the Euler equation (or the divergence thereof) takes the form:

$$\begin{aligned} \partial_{\eta}\Theta + \frac{\partial_{\eta}a}{a}\Theta + \partial_i(v^j \nabla_j v^i) &= -4\pi G \bar{\rho} a^2 \delta \\ + \frac{1}{4a^2 \bar{m}^2} \nabla^2 \left(\nabla^2 \delta - \frac{1}{4} \nabla^2 \delta^2 - \frac{1}{2} \delta \nabla^2 \delta + \dots \right) & \quad (\text{B15}) \end{aligned}$$

The first line of the equation is exactly the Euler equation in the usual CDM case (pressureless fluid), where the term on the right accounts for the effect of gravity – it tends to make Θ negative (i.e. convergent flow). The second line represents the effect of quantum pressure. Its linear contribution (i.e. $\propto \nabla^2 \nabla^2 \delta$) counteracts the effect of gravity. As an illustration, consider a density peak with $\delta > 0$ such as the one shown in Fig 13; the sign of the linear quantum pressure term (i.e. $-\nabla^2 p \propto \nabla^2 \nabla^2 \delta$) is opposite to that of the gravity term (i.e. $-4\pi G \bar{\rho} a^2 \delta$) at the top of the peak. This is precisely the Jeans phenomenon in linear theory. *On the other hand, the quadratic terms from the quantum pressure acts in the same direction as*

gravity! As demonstrated in Fig. 13, the linear order of $-\nabla^2 p$ (dashed line) is positive at the center which counteracts the gravity. However, the exact evaluation of nonlinear $-\nabla^2 p$ (solid line) is actually negative and enhances the gravitational collapse (close to the density peak). The density profile chosen is admittedly artificial, but it serves to illustrate the point that quantum pressure needs not always oppose fluctuation growth. Thus while the fuzziness of dark matter leads to a suppression of the *linear* power on scales smaller than the Jeans scale (see below), the reverse could happen in the *nonlinear* regime. This is borne out by numerical simulations, showing that nonlinear halos often have large density fluctuations due to the accidental interference of waves (references). In this section, we have a relatively narrow goal: compute the one-loop perturbative corrections to the linear (tree) power spectrum, which requires following the perturbation evolution up to cubic order. We will see that the quantum pressure in the end leads to a suppression of power for this particular quantity.

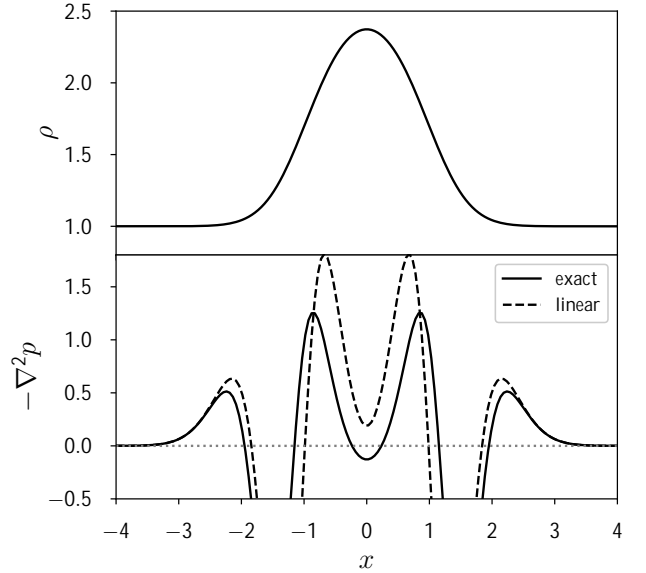


FIG. 13. $-\nabla^2 p$ for a density profile $\rho = [1 + (1 + 0.85 \exp x^2)^{-1}]^2$. The plot is drawn with $4\pi G$, a and \bar{m} all set to unity. The exact value of $-\nabla^2 p$ is negative at the center, so the quantum pressure actually enhances gravitational collapse (around the center). However, the linear perturbative term is positive and acts to slow down the collapse.

Eqn. (B7) can be solved perturbatively, assuming small perturbations. Suppose $\Psi_a = \Psi_a^{(1)} + \Psi_a^{(2)} + \Psi_a^{(3)} + \dots$ where $\Psi_a^{(2)}$ is of the same order as $[\Psi_a^{(1)}]^2$, etc. The first order (linear) solution is

$$\begin{bmatrix} \Psi_1^{(1)}(\mathbf{k}, \bar{\eta}) \\ \Psi_2^{(1)}(\mathbf{k}, \bar{\eta}) \end{bmatrix} = \begin{bmatrix} D_k(\bar{\eta}) \\ -\partial_{\bar{\eta}} D_k(\bar{\eta}) \end{bmatrix} \delta^{(1)}(\mathbf{k}, \bar{\eta}_{\text{in}}), \quad (\text{B16})$$

where we have made the time dependence explicit, and $\bar{\eta}_{\text{in}}$ is some early time (that can be sent to 0). The linear growth factor $D_k(\bar{\eta})$ satisfies the equation:

$$\partial_{\bar{\eta}}^2 D_k + \frac{2}{\bar{\eta}} \partial_{\bar{\eta}} D_k - \left(\frac{6}{\bar{\eta}^2} - \frac{b_k^2}{\bar{\eta}^4} \right) D_k = 0, \quad (\text{B17})$$

and is given by:

$$D_k(\bar{\eta}) = \sqrt{\frac{\bar{\eta}_{\text{in}}}{\bar{\eta}}} \frac{J_{-5/2}(b_k/\bar{\eta})}{J_{-5/2}(b_k/\bar{\eta}_{\text{in}})}, \quad (\text{B18})$$

where $J_{-5/2}$ is the Bessel function:

$$J_{-5/2}(z) \equiv \sqrt{\frac{2}{\pi z}} \left[\frac{3 \cos z}{z^2} + \frac{3 \sin z}{z} - \cos z \right]. \quad (\text{B19})$$

Replacing $J_{-5/2}$ by $J_{5/2}$ would have given the decaying mode, with

$$J_{5/2}(z) \equiv \sqrt{\frac{2}{\pi z}} \left[\frac{3 \sin z}{z^2} - \frac{3 \cos z}{z} - \sin z \right]. \quad (\text{B20})$$

The small z limit of the Bessel functions is:

$$J_{-5/2}(z) \rightarrow \sqrt{\frac{2}{\pi}} \frac{3}{z^{5/2}}, \quad J_{5/2}(z) \rightarrow \sqrt{\frac{2}{\pi}} \frac{z^{5/2}}{15}, \quad (\text{B21})$$

and thus $D_k \propto \bar{\eta}^2$ in the small k limit, as expected. The argument of the Bessel function $b_k/\bar{\eta}$ determines the importance of quantum pressure: when it is large (i.e. $k \gtrsim k_{\text{Jeans}}$), quantum pressure is important and the growth factor $D_k(\bar{\eta})$ is oscillatory with a decaying amplitude.

For an accurate evaluation of the Bessel function, it is best not to use these explicit expressions but rather use recurrence relations (see Numerical Recipe). Going beyond linear theory requires a solution to Eqn. (B17) with a non-vanishing right hand side i.e. the following equation for $u(\bar{\eta})$ for some general source $g(\bar{\eta})$:

$$\partial_{\bar{\eta}}^2 u(\bar{\eta}) + \frac{2}{\bar{\eta}} \partial_{\bar{\eta}} u(\bar{\eta}) - \left(\frac{6}{\bar{\eta}^2} - \frac{b_k^2}{\bar{\eta}^4} \right) u(\bar{\eta}) = g(\bar{\eta}) \quad (\text{B22})$$

can be solved by (up to the addition of a homogenous solution):

$$u(\bar{\eta}) = \int_{\bar{\eta}_{\text{in}}}^{\bar{\eta}} ds g(s) G_k(s, \bar{\eta}), \quad (\text{B23})$$

where $G_k(s, \bar{\eta})$ is the propagator:

$$G_k(s, \bar{\eta}) = \frac{\pi s^2}{2} \left[s^{-1/2} J_{5/2}(b_k/s) \bar{\eta}^{-1/2} J_{-5/2}(b_k/\bar{\eta}) - \bar{\eta}^{-1/2} J_{5/2}(b_k/\bar{\eta}) s^{-1/2} J_{-5/2}(b_k/s) \right]. \quad (\text{B24})$$

It is useful to note that $G_k(\bar{\eta}, \bar{\eta}) = 0$ and:

$$\begin{aligned} \partial_{\bar{\eta}} G_k(s, \bar{\eta}) \Big|_{s=\bar{\eta}} &= 1 \\ \partial_s G_k(s, \bar{\eta}) \Big|_{s=\bar{\eta}} &= -1 \\ G_{k \rightarrow 0}(s, \bar{\eta}) &= \frac{1}{5} \left(\frac{\bar{\eta}^2}{s} - \frac{s^4}{\bar{\eta}^3} \right). \end{aligned} \quad (\text{B25})$$

With these definitions in place, Eqn. (B17) has the following formal solution:

$$\begin{aligned} \Psi_a(\mathbf{k}, \bar{\eta}) &= \Psi_a^{(1)}(\mathbf{k}, \bar{\eta}) \\ &+ \int \frac{d^3 k_1 d^3 k_2}{(2\pi)^3} \delta_D(\mathbf{k} - \mathbf{k}_{12}) \\ &\int_{\bar{\eta}_{\text{in}}}^{\bar{\eta}} ds W_{abc}(\mathbf{k}, \mathbf{k}_1, \mathbf{k}_2; s, \bar{\eta}) \Psi_b(\mathbf{k}_1, s) \Psi_c(\mathbf{k}_2, s) \\ &+ \int \frac{d^3 k_1 d^3 k_2 d^3 k_3}{(2\pi)^6} \delta_D(\mathbf{k} - \mathbf{k}_{123}) \\ &\int_{\bar{\eta}_{\text{in}}}^{\bar{\eta}} ds U_{abcd}(\mathbf{k}, \mathbf{k}_1, \mathbf{k}_2, \mathbf{k}_3; s, \bar{\eta}) \\ &\Psi_b(\mathbf{k}_1, s) \Psi_c(\mathbf{k}_2, s) \Psi_d(\mathbf{k}_3, s) \\ &+ \dots, \end{aligned} \quad (\text{B26})$$

where the ellipsis represents terms with products of four Ψ 's or more. The kernels W and U are defined by:

$$\begin{aligned} W_{1bc}(\mathbf{k}, \mathbf{k}_1, \mathbf{k}_2; s, \bar{\eta}) &\equiv \left(-\gamma_{1bc}(\mathbf{k}, \mathbf{k}_1, \mathbf{k}_2; s) \partial_s \right. \\ &\left. -\gamma_{2bc}(\mathbf{k}, \mathbf{k}_1, \mathbf{k}_2; s) + \frac{2}{s} \gamma_{1bc}(\mathbf{k}, \mathbf{k}_1, \mathbf{k}_2; s) \right) G_k(s, \bar{\eta}), \\ W_{2bc}(\mathbf{k}, \mathbf{k}_1, \mathbf{k}_2; s, \bar{\eta}) &\equiv \left(\gamma_{2bc}(\mathbf{k}, \mathbf{k}_1, \mathbf{k}_2; s) \right. \\ &\left. -\frac{2}{s} \gamma_{1bc}(\mathbf{k}, \mathbf{k}_1, \mathbf{k}_2; s) + \gamma_{1bc}(\mathbf{k}, \mathbf{k}_1, \mathbf{k}_2; s) \partial_s \right) \partial_{\bar{\eta}} G_k(s, \bar{\eta}), \\ U_{1bcd}(\mathbf{k}, \mathbf{k}_1, \mathbf{k}_2, \mathbf{k}_3; s, \bar{\eta}) &= \\ &-\Gamma_{2bcd}(\mathbf{k}, \mathbf{k}_1, \mathbf{k}_2, \mathbf{k}_3; s) G_k(s, \bar{\eta}), \\ U_{2bcd}(\mathbf{k}, \mathbf{k}_1, \mathbf{k}_2, \mathbf{k}_3; s, \bar{\eta}) &= \\ &\Gamma_{2bcd}(\mathbf{k}, \mathbf{k}_1, \mathbf{k}_2, \mathbf{k}_3; s) \partial_{\bar{\eta}} G_k(s, \bar{\eta}), \end{aligned} \quad (\text{B27})$$

where the implicit time dependence of γ and Γ is made explicit for clarity. Eqn. (B26) can be used to obtain the perturbative solution iteratively: plugging in $\Psi = \Psi^{(1)}$ to the right gives $\Psi^{(1)} + \Psi^{(2)}$ (ignoring third order terms and higher); plugging in $\Psi = \Psi^{(1)} + \Psi^{(2)}$ to the right gives $\Psi^{(1)} + \Psi^{(2)} + \Psi^{(3)}$ (ignoring fourth order terms and higher).

We are primarily interested in the density (equal-time) power spectrum $P(k, \bar{\eta})$:

$$\langle \Psi_1(\mathbf{k}, \bar{\eta}) \Psi_1(\mathbf{k}', \bar{\eta}) \rangle \equiv (2\pi)^3 \delta_D(\mathbf{k} + \mathbf{k}') P(k, \bar{\eta}). \quad (\text{B28})$$

The linear (or tree) power spectrum $P^{(11)}$ is given by

$$\langle \Psi_1^{(1)}(\mathbf{k}, \bar{\eta}) \Psi_1^{(1)}(\mathbf{k}', \bar{\eta}) \rangle \equiv (2\pi)^3 \delta_D(\mathbf{k} + \mathbf{k}') P^{(11)}(k, \bar{\eta}), \quad (\text{B29})$$

and can be expressed in terms of the initial tree power times the growth factors:

$$P^{(11)}(k, \bar{\eta}) = P^{(11)}(k, \bar{\eta}_{\text{in}}) D_k(\bar{\eta})^2 / D_k(\bar{\eta}_{\text{in}})^2. \quad (\text{B30})$$

The tree power spectrum at redshift $z = 5$ for an FDM particle mass of 10^{-23} eV is shown in the lower panel of Fig. 1 (the lower dashed line). The tree power spectrum at the same redshift and with the same initial condition but CDM dynamics is shown as the lower solid line in the

same panel. The fact that they are very similar is due to the fact that the growth factor D_k does not differ a whole lot between FDM and CDM dynamics for $k < 10$ h/Mpc. (Recall from Eqn. (B14) that $k_{\text{Jeans}} \sim 14/\text{Mpc}$ for a mass of 10^{-23} eV.) In other words, the suppression of power seen in Fig. 1 at high momenta has nothing to do with the low redshift FDM dynamics; it's all in the initial condition. Indeed, the scale at which the initial power spectrum is suppressed by a factor of two is:

$$k_{1/2} = 1.62/\text{Mpc} \left(\frac{m}{10^{-23} \text{ eV}} \right)^{4/9}. \quad (\text{B31})$$

This is substantially smaller (i.e. larger scale) compared to k_{Jeans} at $z = 5$. Thus, based on linear perturbation theory alone, we do not expect CDM and FDM dynamics to give vastly different power spectra starting from the same initial condition. The question is whether this persists at higher order.

There are two lowest order perturbative corrections (the so called loop corrections) $P^{(22)}$ and $P^{(13)}$, i.e.

$$P(k, \bar{\eta}) = P^{(11)}(k, \bar{\eta}) + P^{1\text{-loop}}(k, \bar{\eta}), \quad (\text{B32})$$

with $P^{1\text{-loop}} \equiv P^{(22)} + P^{(13)}$, are given by:

$$\langle \Psi_1^{(2)}(\mathbf{k}, \bar{\eta}) \Psi_1^{(2)}(\mathbf{k}', \bar{\eta}) \rangle \equiv (2\pi)^3 \delta_D(\mathbf{k} + \mathbf{k}') P^{(22)}(k, \bar{\eta}), \quad (\text{B33})$$

$$\langle \Psi_1^{(1)}(\mathbf{k}, \bar{\eta}) \Psi_1^{(3)}(\mathbf{k}', \bar{\eta}) \rangle + \langle \Psi_1^{(3)}(\mathbf{k}, \bar{\eta}) \Psi_1^{(1)}(\mathbf{k}', \bar{\eta}) \rangle \\ \equiv (2\pi)^3 \delta_D(\mathbf{k} + \mathbf{k}') P^{(13)}(k, \bar{\eta}) \quad (\text{B34})$$

It can be shown the loop correction $P^{(22)}$ takes the form:

$$P^{(22)}(k, \bar{\eta}) = 2 \int \frac{d^3 k_1 d^3 k_2}{(2\pi)^3} \delta_D(\mathbf{k} - \mathbf{k}_{12}) F_{\text{II}}(\mathbf{k}_1, \mathbf{k}_2, \bar{\eta})^2 \\ P^{(11)}(k_1, \bar{\eta}) P^{(11)}(k_2, \bar{\eta}), \quad (\text{B35})$$

where the kernel F_{II} is defined by

$$F_{\text{II}}(\mathbf{k}_1, \mathbf{k}_2, \bar{\eta}) \equiv \int_{\bar{\eta}_{\text{in}}}^{\bar{\eta}} ds W_{1bc}(\mathbf{k}_{12}, \mathbf{k}_1, \mathbf{k}_2; s, \bar{\eta}) \\ f_b(k_1, s, \bar{\eta}) f_c(k_2, s, \bar{\eta}), \quad (\text{B36})$$

with f_b, f_c defined by

$$f_1(k, s, \bar{\eta}) \equiv D_k(s)/D_k(\bar{\eta}) \\ f_2(k, s, \bar{\eta}) \equiv -\partial_s D_k(s)/D_k(\bar{\eta}). \quad (\text{B37})$$

This F_{II} is often referred to as F_2 in the literature (or the symmetrized version thereof) and matches that in the $k \rightarrow 0$ limit (or $\bar{m} \rightarrow \infty$). Numerically, it is advantageous to compute $P^{(22)}$ by rewriting the integral in Eqn. (B35) as:

$$P^{(22)}(k, \bar{\eta}) = 4 \int_{k_1 \leq |\mathbf{k} - \mathbf{k}_1|} \frac{d^3 k_1}{(2\pi)^3} F_{\text{II}}(\mathbf{k}_1, \mathbf{k} - \mathbf{k}_1, \bar{\eta})^2 \\ P^{(11)}(k_1, \bar{\eta}) P^{(11)}(|\mathbf{k} - \mathbf{k}_1|, \bar{\eta}), \quad (\text{B38})$$

where the restriction of $k_1 \leq |\mathbf{k} - \mathbf{k}_1|$ implies a restriction on the angle between \mathbf{k} and \mathbf{k}_1 if $k_1 > k/2$. This way of integrating avoids divergent terms in F that go as $k^2/|\mathbf{k} - \mathbf{k}_1|^2$ when $|\mathbf{k} - \mathbf{k}_1|$ becomes small [43]. Terms that diverge as k^2/k_1^2 as k_1 becomes small are harmless because of the integration measure $d^3 k_1$. (In fact, even $O(k/k_1)$ terms in F can be avoided by a further rewriting.) It is also to note that $F_{\text{II}}(\mathbf{k}_1, \mathbf{k}_2, \bar{\eta}) = 0$ if $\mathbf{k}_1 + \mathbf{k}_2 = 0$, because the corresponding kernels γ_{abc} 's vanish in that case.

The other loop correction to the power spectrum $P^{(13)}$, which is of the same order as $P^{(22)}$, is given by

$$P^{(13)}(k, \bar{\eta}) = \int \frac{d^3 k_2}{(2\pi)^3} \left(4F_{\text{III}}(\mathbf{k}_2, -\mathbf{k}_2, \mathbf{k}, \bar{\eta}) + \right. \\ \left. + 2H_{\text{III}}(\mathbf{k}, \mathbf{k}_2, \bar{\eta}) \right) P^{(11)}(k, \bar{\eta}) P^{(11)}(k_2, \bar{\eta}), \quad (\text{B39})$$

where the kernel F_{III} is defined by

$$F_{\text{III}}(\mathbf{k}_2, \mathbf{k}'_1, \mathbf{k}'_2, \bar{\eta}) \equiv 2 \int_0^{\bar{\eta}} ds W_{1bc}(\mathbf{k}_{12}, \mathbf{k}_1, \mathbf{k}_2; s, \bar{\eta}) \\ \int_0^s ds' W_{bb'c'}(\mathbf{k}_1, \mathbf{k}'_1, \mathbf{k}'_2; s', s) f_{b'}(k'_1, s', \bar{\eta}) \\ f_{c'}(k'_2, s', \bar{\eta}) f_c(k_2, s, \bar{\eta}), \quad (\text{B40})$$

where $\mathbf{k}_1 = \mathbf{k}'_1 + \mathbf{k}'_2$. Note that $F_{\text{III}}(\mathbf{k}_2, \mathbf{k}'_1, \mathbf{k}'_2, \bar{\eta}) = 0$ if $\mathbf{k}'_1 + \mathbf{k}'_2 = 0$ because $W_{abc}(\mathbf{k}_{12}, \mathbf{k}_1, \mathbf{k}_2; s, \bar{\eta}) = 0$ in the case $\mathbf{k}_{12} = 0$. This is why a term that goes like $F_{\text{III}}(\mathbf{k}, \mathbf{k}_2, -\mathbf{k}_2, \bar{\eta})$ is absent from Eqn. (B39). A common convention in the literature is to use a fully symmetrized version of F_{III} in which case such a term would be present.¹⁰

The kernel H_{III} is given by:

$$H_{\text{III}}(\mathbf{k}, \mathbf{k}_2, \bar{\eta}) \equiv f_a(k, \bar{\eta}, \bar{\eta}) \int_{\bar{\eta}_{\text{in}}}^{\bar{\eta}} ds \\ \left(U_{abcd}(\mathbf{k}, \mathbf{k}_2, -\mathbf{k}_2, \mathbf{k}; s, \bar{\eta}) f_b(k_2, s, \bar{\eta}) f_c(k_2, s, \bar{\eta}) f_d(k, s, \bar{\eta}) \right. \\ \left. + U_{abcd}(\mathbf{k}, \mathbf{k}_2, \mathbf{k}, -\mathbf{k}_2; s, \bar{\eta}) f_b(k_2, s, \bar{\eta}) f_c(k, s, \bar{\eta}) f_d(k_2, s, \bar{\eta}) \right. \\ \left. + U_{abcd}(\mathbf{k}, \mathbf{k}, \mathbf{k}_2, -\mathbf{k}_2; s, \bar{\eta}) f_b(k, s, \bar{\eta}) f_c(k_2, s, \bar{\eta}) f_d(k_2, s, \bar{\eta}) \right). \quad (\text{B41})$$

Fig. 1 lower panel shows the total power ($P^{11} + P^{22} + P^{13}$) computed this way: the upper solid line uses CDM dynamics while the upper dashed line uses FDM dynamics (same initial condition). The power is enhanced at high momenta compared with the tree power spectrum

¹⁰ In other words, the general structure should be to replace $4F_{\text{III}}$ in Eqn. (B39) by $2F_{\text{III}}(\mathbf{k}_2, -\mathbf{k}_2, \mathbf{k}) + 2F_{\text{III}}(\mathbf{k}_2, \mathbf{k}, -\mathbf{k}_2) + 2F_{\text{III}}(\mathbf{k}, \mathbf{k}_2, -\mathbf{k}_2)$. The last contribution vanishes as argued above. The second term matches the first i.e. $F_{\text{III}}(\mathbf{k}_2, -\mathbf{k}_2, \mathbf{k}) = F_{\text{III}}(\mathbf{k}_2, \mathbf{k}, -\mathbf{k}_2)$, which is guaranteed by the fact that $W_{bb'c'}(\mathbf{k}_1, \mathbf{k}'_1, \mathbf{k}'_2) = W_{bc'b'}(\mathbf{k}_1, \mathbf{k}'_2, \mathbf{k}'_1)$. If one were to use a fully symmetrized version of the kernel, one would have replaced $4F_{\text{III}}$ by $6F_{\text{III}}^{\text{symm}}$.

(the lower solid/dashed lines). The power at $k \gtrsim k_{1/2}$ comes almost entirely from transferred power from large scales (low momenta). Just as in the case of the tree power, CDM vs FDM dynamics does not appear to make a big difference in the total power. The total power with FDM dynamics is slightly lower than that with CDM dynamics, except possibly at $k \sim 10$ h/Mpc, though at that point, the power spectrum is rather low in any case.

Fig. 1 upper panel compares the total power in two cases (both with FDM dynamics): the dashed line is the same as the black dashed line in the lower panel; the dotted line shows the power computed using Eqn. (B38) and (B39) with an infrared cut-off of the loop momentum at $2\pi/10$ h/Mpc. The latter is chosen to mimic the effect of having a finite simulation box of size 10 Mpc/h. One can see the transferred power from large scales is diminished, because the relevant large scale modes are absent in a finite box.

Lastly, let's note that the bispectrum B , defined by

$$\begin{aligned} & (\Psi_1(\mathbf{k}_1, \bar{\eta})\Psi_1(\mathbf{k}_2, \bar{\eta})\Psi_1(\mathbf{k}_3, \bar{\eta}) \equiv \\ & (2\pi)^3 \delta_D(\mathbf{k}_1 + \mathbf{k}_2 + \mathbf{k}_3) B(\mathbf{k}_1, \mathbf{k}_2, \mathbf{k}_3, \bar{\eta}), \end{aligned} \quad (\text{B42})$$

is given, to the lowest order in perturbation theory, by:

$$\begin{aligned} B(\mathbf{k}_1, \mathbf{k}_2, \mathbf{k}_3, \bar{\eta}) = & \\ & 2F_{II}(\mathbf{k}_1, \mathbf{k}_2, \bar{\eta})P^{(11)}(k_1, \bar{\eta})P^{(11)}(k_2, \bar{\eta}) + \\ & 2F_{II}(\mathbf{k}_2, \mathbf{k}_3, \bar{\eta})P^{(11)}(k_2, \bar{\eta})P^{(11)}(k_3, \bar{\eta}) + \\ & 2F_{II}(\mathbf{k}_3, \mathbf{k}_1, \bar{\eta})P^{(11)}(k_3, \bar{\eta})P^{(11)}(k_1, \bar{\eta}). \end{aligned} \quad (\text{B43})$$

Appendix C: Wave Perturbation Theory

Instead of the fluid equations, one could instead consider the wave formulation:

$$i \left(\partial_t \psi + \frac{3}{2} H \psi \right) = \left(-\frac{\nabla^2}{2\bar{m}a^2} + \bar{m}\Phi \right) \psi, \quad (\text{C1})$$

supplemented by the Poisson equation (B3). Here, t is the proper time, and H is the Hubble constant $\partial_t a/a$.

The density δ is related to ψ by

$$\delta = \frac{|\psi|^2 - |\bar{\psi}|^2}{|\bar{\psi}|^2}, \quad (\text{C2})$$

where $\bar{\psi}$ is the cosmic mean and can be taken to be real. The velocity \mathbf{v} can be deduced from

$$(1 + \delta)\mathbf{v} = \frac{1}{2ia\bar{m}|\bar{\psi}|^2} (\psi^* \nabla \psi - \psi \nabla \psi^*). \quad (\text{C3})$$

Let us contrast wave perturbation theory with fluid perturbation theory. For the latter, we assume δ is small, in which case the linearized mass conservation equation tells us, in momentum space:

$$v \sim k^{-1} (\partial_\eta D_k / D_k) \delta \sim \frac{aH}{k} \delta \quad (\text{C4})$$

where, in the last equality, we assume the growth factor $D_k \sim a$, appropriate for low momenta. Thus, as long as the wavelength of interest is sub-Hubble ($k > aH$) which is almost always the case, a small δ implies a small v as well.

For wave perturbation theory, we assume $\delta\psi \equiv \psi - \bar{\psi}$ is small. It turns out this breaks down earlier (at higher redshift) than the break down of small δ and v . Let us relate δ and v to the first order perturbation in ψ :

$$\delta = (\delta\psi + \delta\psi^*)/\bar{\psi}, \quad (\text{C5})$$

and

$$\mathbf{v} = \frac{1}{2ia\bar{m}\bar{\psi}} \nabla (\delta\psi - \delta\psi^*) \quad (\text{C6})$$

The smallness of δ is thus equivalent to the smallness of $(\delta\psi + \delta\psi^*)/\bar{\psi}$. It does not automatically guarantee that $(\delta\psi - \delta\psi^*)/\bar{\psi}$ is also small. In momentum space, $(\delta\psi - \delta\psi^*)/\bar{\psi}$ can be written as

$$\frac{\delta\psi - \delta\psi^*}{\bar{\psi}} \sim \frac{a\bar{m}v}{k} \sim \frac{a^2\bar{m}H}{k^2} \delta, \quad (\text{C7})$$

where we have used linearized mass conservation in the last equality. We see that the smallness of $(\delta\psi - \delta\psi^*)/\bar{\psi}$ is much more demanding than the smallness of v : we need $a^2\bar{m}H < k^2$ which is roughly $k_{\text{Jeans}} < k$. In other words, for wave perturbation theory to work, it is not sufficient for δ to be small; one needs $(k_{\text{Jeans}}/k)^2 \delta$ to be small. If the length scale of interest is above Jeans scale $k < k_{\text{Jeans}}$, one would need a *very* small δ to compensate (i.e. by going to an earlier time).¹¹

Thus it appears wave perturbation theory has a rather limited range of applicability. A corollary of the above reasoning is that a numerical simulation of the wave equations is also very demanding on resolution: suppose one is interested in simulating structure growth on some large length scale (small $k \sim k_0$). The typical velocity on such a scale is $v \sim (aH/k_0)\delta$. Accounting for the typical power spectrum for δ , this velocity generally becomes larger as k_0 becomes smaller. The velocity shows up in a wave simulation as the gradient of the phase of ψ . It is important that the wave simulation resolves the de Broglie wavelength associated with this velocity i.e. $k_{\text{resolution}} \sim a\bar{m}v$. Thus, a wave simulation requires high resolution even if the length scale of interest is large.

The wave description is perhaps more useful in the highly nonlinear regime, where δ is large but v remains modest. The velocity information is repackaged into the phase of the ψ in such a way that the wave equation is linear in the absence of gravity. Contrast this with the fluid equations which are nonlinear even if gravity is turned off. How to take advantage of the fluid-wave mapping to gain insight into nonlinear clustering is a topic for further investigation.

¹¹ We thank Michael Landry and Alberto Nicolis for discussions regarding wave perturbation theory.

ACKNOWLEDGMENTS

We thank Marco Baldi, Zoltan Haiman, Vid Iršič, Michael Landry, Alberto Nicolis, Jerry Ostriker, Massimo Pietroni, Roman Scoccimarro, Sergey Sibiryakov and Matteo Viel for useful discussions. We gratefully recognize computational resources provided by NSF XSEDE through grant number TGMCA99S024, the NASA High-End Computing Program through the NASA Advanced Supercomputing Division at Ames Research Center, Columbia University, and the Flatiron Institute. This

work made significant use of many open source software packages, including yt, Enzo, Python, IPython, NumPy, SciPy, Matplotlib, HDF5, h5py. These are products of collaborative effort by many independent developers from numerous institutions around the world. Their commitment to open science has helped to make this work possible. G.L.B. acknowledges support from the NSF (AST-161955) and NASA (NNX15AB20G). L.H. and X.L. acknowledge support from NASA (NXX16AB27G) and DOE (DE-SC011941), and thank Andy Cohen, Henry Tye and the Institute for Advanced Study at the Hong Kong University of Science and Technology for hospitality.

-
- [1] M. R. Baldeschi, R. Ruffini, and G. B. Gelmini, *Phys. Lett.* **122B**, 221 (1983).
- [2] W. Hu, R. Barkana, and A. Gruzinov, *Phys. Rev. Lett.* **85**, 1158 (2000), arXiv:astro-ph/0003365 [astro-ph].
- [3] J. Lesgourgues, A. Arbey, and P. Salati, *New Astron. Rev.* **46**, 791 (2002).
- [4] L. Amendola and R. Barbieri, *Phys. Lett.* **B642**, 192 (2006), arXiv:hep-ph/0509257 [hep-ph].
- [5] P.-H. Chavanis, *Phys. Rev.* **D84**, 043531 (2011), arXiv:1103.2050 [astro-ph.CO].
- [6] A. Arvanitaki, S. Dimopoulos, S. Dubovsky, N. Kaloper, and J. March-Russell, *Phys. Rev.* **D81**, 123530 (2010), arXiv:0905.4720 [hep-th].
- [7] D. J. E. Marsh, *Phys. Rept.* **643**, 1 (2016), arXiv:1510.07633 [astro-ph.CO].
- [8] L. Hui, J. P. Ostriker, S. Tremaine, and E. Witten, *Phys. Rev.* **D95**, 043541 (2017), arXiv:1610.08297 [astro-ph.CO].
- [9] P. Svrcek and E. Witten, *JHEP* **06**, 051 (2006), arXiv:hep-th/0605206 [hep-th].
- [10] H.-Y. Schive, T. Chiueh, and T. Broadhurst, *Nature Phys.* **10**, 496 (2014), arXiv:1406.6586 [astro-ph.GA].
- [11] H.-Y. Schive, M.-H. Liao, T.-P. Woo, S.-K. Wong, T. Chiueh, T. Broadhurst, and W. Y. P. Hwang, *Phys. Rev. Lett.* **113**, 261302 (2014), arXiv:1407.7762 [astro-ph.GA].
- [12] P. Mocz and S. Succi, *Phys. Rev.* **E91**, 053304 (2015), arXiv:1503.03869 [physics.comp-ph].
- [13] B. Schwabe, J. C. Niemeyer, and J. F. Engels, *Phys. Rev.* **D94**, 043513 (2016), arXiv:1606.05151 [astro-ph.CO].
- [14] J. Veltmaat and J. C. Niemeyer, *Phys. Rev.* **D94**, 123523 (2016), arXiv:1608.00802 [astro-ph.CO].
- [15] P. Mocz, M. Vogelsberger, V. Robles, J. Zavala, M. Boylan-Kolchin, and L. Hernquist, *Mon. Not. Roy. Astron. Soc.* **471**, 4559 (2017), arXiv:1705.05845 [astro-ph.CO].
- [16] S.-C. Lin, H.-Y. Schive, S.-K. Wong, and T. Chiueh, *Phys. Rev.* **D97**, 103523 (2018), arXiv:1801.02320 [astro-ph.CO].
- [17] J. Veltmaat, J. C. Niemeyer, and B. Schwabe, *Phys. Rev.* **D98**, 043509 (2018), arXiv:1804.09647 [astro-ph.CO].
- [18] M. Nori and M. Baldi, (2018), arXiv:1801.08144 [astro-ph.CO].
- [19] E. Madelung, *Zeitschrift für Physik* **40**, 322 (1927).
- [20] R. P. Feynman, *Reading, Ma.: Addison-Wesley, 1965, edited by Feynman, Richard P.; Leighton, Robert B.; Sands, Matthew* (1965).
- [21] P. Mocz, L. Lancaster, A. Fialkov, F. Becerra, and P.-H. Chavanis, *Phys. Rev.* **D97**, 083519 (2018), arXiv:1801.03507 [astro-ph.CO].
- [22] J. Zhang, J.-L. Kuo, H. Liu, Y.-L. S. Tsai, K. Cheung, and M.-C. Chu, (2017), arXiv:1708.04389 [astro-ph.CO].
- [23] V. Iri, M. Viel, M. G. Haehnelt, J. S. Bolton, and G. D. Becker, *Phys. Rev. Lett.* **119**, 031302 (2017), arXiv:1703.04683 [astro-ph.CO].
- [24] E. Armengaud, N. Palanque-Delabrouille, C. Yche, D. J. E. Marsh, and J. Baur, *Mon. Not. Roy. Astron. Soc.* **471**, 4606 (2017), arXiv:1703.09126 [astro-ph.CO].
- [25] M. Nori, R. Murgia, V. Iri, M. Baldi, and M. Viel, (2018), arXiv:1809.09619 [astro-ph.CO].
- [26] G. L. Bryan *et al.* (ENZO), *Astrophys. J. Suppl.* **211**, 19 (2014), arXiv:1307.2265 [astro-ph.IM].
- [27] M. J. Turk, B. D. Smith, J. S. Oishi, S. Skory, S. W. Skillman, T. Abel, and M. L. Norman, *ApJS* **192**, 9 (2011), arXiv:1011.3514 [astro-ph.IM].
- [28] R. A. C. Croft, D. H. Weinberg, N. Katz, and L. Hernquist, *Astrophys. J.* **495**, 44 (1998), arXiv:astro-ph/9708018 [astro-ph].
- [29] L. Hui, *Astrophys. J.* **516**, 519 (1999), arXiv:astro-ph/9807068 [astro-ph].
- [30] R. A. C. Croft, D. H. Weinberg, M. Bolte, S. Burles, L. Hernquist, N. Katz, D. Kirkman, and D. Tytler, *Astrophys. J.* **581**, 20 (2002), arXiv:astro-ph/0012324 [astro-ph].
- [31] P. McDonald *et al.* (SDSS), *Astrophys. J.* **635**, 761 (2005), arXiv:astro-ph/0407377 [astro-ph].
- [32] M. Viel, M. G. Haehnelt, and A. Lewis, *Mon. Not. Roy. Astron. Soc.* **370**, L51 (2006), arXiv:astro-ph/0604310 [astro-ph].
- [33] M. Viel, G. D. Becker, J. S. Bolton, and M. G. Haehnelt, *Phys. Rev.* **D88**, 043502 (2013), arXiv:1306.2314 [astro-ph.CO].
- [34] N. Y. Gnedin and L. Hui, *Mon. Not. Roy. Astron. Soc.* **296**, 44 (1998), arXiv:astro-ph/9706219 [astro-ph].
- [35] L. Hui and N. Y. Gnedin, *Mon. Not. Roy. Astron. Soc.* **292**, 27 (1997), arXiv:astro-ph/9612232 [astro-ph].
- [36] J. M. Stone and M. L. Norman, *Astrophys. J. Suppl.* **80**, 753 (1992).
- [37] J. M. Stone and M. L. Norman, *Astrophys. J. Suppl.* **80**, 791 (1992).
- [38] J. N. Fry, *Astrophys. J.* **279**, 499 (1984).

- [39] M. H. Goroff, B. Grinstein, S. J. Rey, and M. B. Wise, *Astrophys. J.* **311**, 6 (1986).
- [40] F. Bernardeau, *Astrophys. J.* **392**, 1 (1992).
- [41] R. Scoccimarro, *Astrophys. J.* **487**, 1 (1997), arXiv:astro-ph/9612207 [astro-ph].
- [42] F. Bernardeau, S. Colombi, E. Gaztanaga, and R. Scoccimarro, *Phys. Rept.* **367**, 1 (2002), arXiv:astro-ph/0112551 [astro-ph].
- [43] J. J. M. Carrasco, S. Foreman, D. Green, and L. Senatore, *JCAP* **1407**, 056 (2014), arXiv:1304.4946 [astro-ph.CO].